Src-dependent phosphorylation of caveolin-1 Tyr-14 promotes swelling and release of caveolae

Adriana M. Zimnicka[a], Yawer S. Husain[a], Ayesha N. Shajahan[a], Maria Sverdlov[a], Oleg Chaga[a], Zhenlong Chen[b], Peter T. Toth[a], Jennifer Klomp[a], Andrei V. Karginov[a], Chinnaswamy Tiruppathi[a], Asrar B. Malik[a,c], and Richard D. Minshall[a,b,c,*]

[a]Department of Pharmacology, [b]Department of Anesthesiology, and [c]Center for Lung and Vascular Biology, College of Medicine, University of Illinois at Chicago, Chicago, IL 60612

ABSTRACT **Caveolin 1 (Cav1) is a required structural component of caveolae, and its phosphorylation by Src is associated with an increase in caveolae-mediated endocytosis. Here we demonstrate, using quantitative live-cell 4D, TIRF, and FRET imaging, that endocytosis and trafficking of caveolae are associated with a Cav1 Tyr-14 phosphorylation-dependent conformational change, which spatially separates, or loosens, Cav1 molecules within the oligomeric caveolar coat. When tracked by TIRF and spinning-disk microscopy, cells expressing phosphomimicking Cav1 (Y14D) mutant formed vesicles that were greater in number and volume than with Y14F-Cav1-GFP. Furthermore, we observed in HEK cells cotransfected with wild-type, Y14D, or Y14F Cav1-CFP and -YFP constructs that FRET efficiency was greater with Y14F pairs than with Y14D, indicating that pY14-Cav1 regulates the spatial organization of Cav1 molecules within the oligomer. In addition, albumin-induced Src activation or direct activation of Src using a rapamycin-inducible Src construct (RapR-Src) led to an increase in monomeric Cav1 in Western blots, as well as a simultaneous increase in vesicle number and decrease in FRET intensity, indicative of a Src-mediated conformational change in CFP/YFP-tagged WT-Cav1 pairs. We conclude that phosphorylation of Cav1 leads to separation or "spreading" of neighboring negatively charged N-terminal phosphotyrosine residues, promoting swelling of caveolae, followed by their release from the plasma membrane.**

Monitoring Editor
Diane Lidke
University of New Mexico

Received: Nov 9, 2015
Revised: Apr 27, 2016
Accepted: May 5, 2016

INTRODUCTION

Caveolae are plasma membrane microdomains that appear as either invaginations open to the extracellular environment or as free cytoplasmic vesicles. They are characterized in both cases by the presence of caveolin-1 (Cav1) and cavin-1/polymerase I and transcript release factor (PTRF) proteins and enrichment in membrane cholesterol. Treatment of cells with methyl-β-cyclodextrin (MβC), a specific cholesterol-binding agent (Rothberg *et al.*, 1992), or knockdown/knockout of Cav1 flattens caveolae or prevents them from forming. Although caveolae are present in most mammalian cell types, in endothelial cells, they comprise nearly 15% of the cell volume (Predescu and Palade, 1993) and account for ~95% of the plasmalemmal vesicles (Predescu *et al.*, 2003). Assessment of caveolae internalization using cholera toxin subunit B, a caveolae-specific tracer that binds to ganglioside GM1 residing in caveolae (Parton *et al.*, 1994), or addition of albumin (Minshall *et al.*, 2000) showed that plasma membrane-bound caveolae internalize receptor-bound and fluid-phase macromolecular cargo by a clathrin-independent mechanism (John *et al.*, 2003; Predescu *et al.*, 2003). Studies in caveolin-1– knockout mice (*Cav1*$^{-/-}$) implicated caveolae as essential for physiological uptake and transport of albumin across vascular endothelia (Schubert *et al.*, 2001; Hu *et al.*, 2008a; Sverdlov *et al.*, 2009), and similar studies in endothelial cells and buffer-perfused organs showed a reduction in ^{125}I-albumin uptake upon treatment of cells with membrane cholesterol–depleting agents MβCD (John *et al.*, 2003) and filipin (John *et al.*, 2001; Vogel *et al.*, 2001). In

This article was published online ahead of print in MBoC in Press (http://www.molbiolcell.org/cgi/doi/10.1091/mbc.E15-11-0756) on May 11, 2016.

*Address correspondence to: Richard D. Minshall (rminsh@uic.edu).

Abbreviations used: Antp, antennapedia; Cav1, caveolin-1; CSD, caveolin-1 scaffold domain; FRET, fluorescence (Förster) resonance energy transfer; HLMVEC, human lung microvascular endothelial cell; MLEC, mouse lung endothelial cell; PP2, 4-amino-5-(4-chlorophenyl)-7-(*t*-butyl)pyrazolo[3,4-*d*]pyrimidine; RLMVEC, rat lung microvascular endothelial cell; TIRF, total internal reflection fluorescence; WT, wild type.

addition, caveolae have been proposed to act as a membrane "buffer" against mechanical stress caused by sudden surges in blood flow or surface stretching of vascular endothelia (Sinha *et al.*, 2011; Parton and del Pozo, 2013).

Cav1, the defining protein constituent of caveolae, was initially identified in a screen for substrates of v-Src kinase (Glenney and Zokas, 1989). Subsequent studies using site-directed mutagenesis and in vitro phosphorylation of Cav1-derived synthetic peptides demonstrated that Cav1 tyrosine 14 (Y14) is the primary phosphorylation site targeted by Src (Li *et al.*, 1996b; Sverdlov *et al.*, 2007). Furthermore, Cav1 phosphorylation in rat lung microvessels after treatment with the general phosphatase inhibitor Na_3VO_4 occurred primarily in endothelial cells of capillaries and venules (Aoki *et al.*, 1999). Immuno–electron microscopy (EM) of phospho-Cav1 versus total Cav1 revealed a reduction in the number of plasma membrane–attached caveolae and a simultaneous increase in the number of cytoplasmic vesicles, suggesting that phosphorylation of Cav1 is associated with formation and/or internalization of caveolae (Nomura and Fujimoto, 1999). Subsequently we showed that expression of DN-Src (Y527F/K295A) mutant in microvascular endothelial cells blocked Cav1 Y14 phosphorylation and reduced albumin uptake (Minshall *et al.*, 2000; Shajahan *et al.*, 2004b). Moreover, Cav1 Y14 phosphorylation was shown to promote transcription of Cav1 and cavin-1 genes in breast carcinoma cells (Joshi *et al.*, 2012) and stimulate caveolae biogenesis in human pancreatic tumor (PANC-1) cells (Orlichenko *et al.*, 2006).

Caveolae-mediated endocytosis of albumin is a selective and regulated process, using a Gαi/βγ-coupled Src kinase signaling pathway (Minshall *et al.*, 2000; Shajahan *et al.*, 2004b) that can be triggered either by binding of native albumin to gp60 located in caveolae or cross-linking with specific anti-gp60 antibody (Tiruppathi *et al.*, 1997). A similar Src-dependent mechanism of endocytosis via caveolae was observed for SV40 virus (Pelkmans *et al.*, 2002), glycosphingolipids such as lactoceramide (Singh *et al.*, 2003), and insulin (Wang *et al.*, 2015). We also showed that ICAM-1 activation by antibody (Ab) cross-linking or activated-neutrophil binding, as well as H_2O_2, can induce caveolae-mediated endocytosis in a Src- and pY14-Cav1–dependent manner (Hu *et al.*, 2008b; Sun *et al.*, 2009).

Posttranslational modification of Cav1 by palmitoylation of C-terminal cysteine residues was proposed to facilitate stable anchorage of Cav1 to the plasma membrane, as well as to promote the association of Src kinase with caveolae via hydrophobic interactions between the myristoyl moiety of Src and palmitoylated cysteine 156 of Cav1 (Lee *et al.*, 2001; Bakhshi *et al.*, 2013). Once associated with caveolae, Src phosphorylates Cav1 on Tyr-14, which then promotes additional binding of Src via its SH2 domain to pY14-Cav1 (Gottlieb-Abraham *et al.*, 2013). In addition, Src phosphorylates dynamin-2 (Ahn *et al.*, 1999), a GTPase that facilitates closure of the caveolar neck and fission of caveolae (Shajahan *et al.*, 2004a). Subsequent movement of caveolae coincides with actin remodeling (Rozelle *et al.*, 2000) and binding of pY14-Cav1 to actin cross-linking protein filamin A (Sverdlov *et al.*, 2009). Of interest, prolonged Cav1 phosphorylation leads to polyubiquitination on lysine 86 and degradation via the proteasome, which we hypothesized contributes to depletion of caveolae (Bakhshi *et al.*, 2013), tolerance to nitroglycerin (Mao *et al.*, 2014), cardiac arrhythmias (Yang *et al.*, 2014), and, as recently reported by the Barrett lab, insulin resistance in rats fed high-fat diet (Wang *et al.*, 2015).

Although Cav1 is a small protein of ~22 kDa in situ, it has been shown to oligomerize into long filaments composed of repeating heptameric rings of Cav1 (Fernandez *et al.*, 2002). Oligomerization of Cav1 and further stabilization by cavin proteins (Kovtun *et al.*, 2014) are critical for membrane invagination into the characteristic flask-shaped caveolar structures that "hang" from the plasma membrane (Rothberg *et al.*, 1992; Monier *et al.*, 1995; Anderson, 1998). Unlike the mechanism of clathrin-dependent endocytosis, in which plasma membrane is forced to invaginate on demand in an orchestrated clathrin/triskelion-dependent manner (Schmid, 1997), caveolin-enriched membrane microdomains are thought of as stably formed, vesicle-like structures that await activation by ligands and macromolecules to induce fission and endocytosis (Tagawa *et al.*, 2005), often in a "kiss-and-run" manner (Pelkmans and Zerial, 2005). Thus endocytosis via caveolae is triggered by Cav1 phosphorylation, closure of the caveolar neck from the extracellular space by dynamin-2, and filamin A/actin-dependent movement of vesicles away from the plasma membrane.

In the present study, we examined the effect of Y14 Cav1 phosphorylation on trafficking dynamics and volume of Cav1-green fluorescent protein (GFP)–positive vesicles using total internal reflection fluorescence (TIRF) and spinning-disk confocal microscopy and on the stability of caveolin oligomers in boiled and nonboiled samples in SDS gels. We also used live-cell fluorescence (Förster) resonance energy transfer (FRET) imaging to assess simultaneously conformational changes in membrane-associated caveolin-1 oligomers and the number of vesicles released upon Cav1 Y14 phosphorylation.

RESULTS

Albumin, a primary macromolecular cargo of caveolae, increases the velocity and volume of Cav1-GFP–positive vesicles via phosphorylation of Cav1 Y14

We used the fast-acquisition capabilities of spinning-disk confocal microscopy to characterize the velocity and volume of trafficking vesicles (Supplemental Figure S1 Movie) and the high resolution of TIRF microscopy (Supplemental Figure S2 Movie) to quantify the number of vesicular fusion/fission events near the basal surface in endothelial cells expressing GFP-tagged constructs of Cav1. The four-dimensional (4D) dynamics (*x*, *y*, *z*, time) of vesicle trafficking was determined by first classifying moving fluorescent objects (Cav1-GFP+) using Volocity particle-tracking software followed by three-dimensional (3D) deconvolution to achieve higher image resolution. We thus measured dynamic changes in location, size, and number of mobile Cav1-GFP+ vesicles over time.

Western blot analysis of RLMVEC lysates indicates that bovine serum albumin (BSA) induced the phosphorylation of Cav1 on Tyr-14 (Y14) within the first 5 min of treatment, and phosphorylation was even greater when BSA was combined with the nonspecific phosphatase inhibitor sodium orthovanadate (Na_3VO_4; Figure 1A). Addition of the Src kinase inhibitor 4-amino-5-(4-chlorophenyl)-7-(*t*-butyl)pyrazolo[3,4-*d*]pyrimidine (PP2) reversed the combined effect of BSA and Na_3VO_4 on Cav1 phosphorylation (Figure 1A). Addition of albumin to serum-starved rat lung microvascular endothelial cells (RLMVECs) expressing GFP-tagged wild-type (WT)-Cav1 (Cav1-GFP+) led to a robust threefold increase in the number of mobile cytoplasmic vesicles within the first 5 min, which persisted for up to 20 min (Figure 1B). Analysis of velocity and volume of tracked Cav1-GFP+ cytoplasmic vesicles indicated that there was a BSA-dependent 2-fold increase in median vesicle velocity (Figure 1C) and a 2.5-fold increase in volume, or "swelling" (Figure 1D and Supplemental Figure S1B). Treatment of cells with the Src kinase inhibitor PP2 prevented BSA-induced swelling of Cav1-GFP+ vesicles and even made the volume slightly smaller than in serum-starved cells, suggesting that there is an effect of residual background phosphorylation (Figure 1D). PP2 tended to block the effect of BSA on

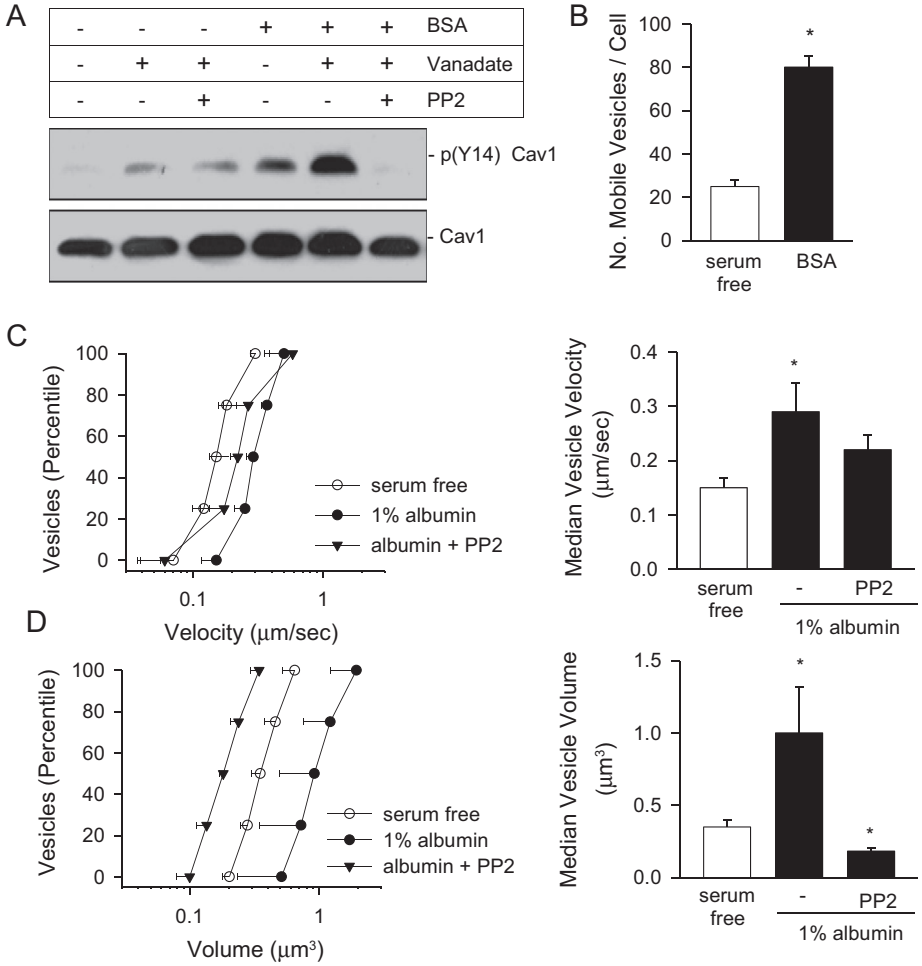

FIGURE 1: BSA increases the number and volume of Cav1-GFP+ vesicles in rat lung microvascular endothelial cells. WT-Cav1-GFP was transfected by electroporation into RLMVECs. At 48 h posttransfection, cells were serum deprived for 3 h and then pretreated for 10 min with 15 μM PP2 or 10 μM Na_3VO_4 as indicated. (A) RLMVECs were stimulated with BSA, lysed, and then analyzed by Western blotting with pY14-Cav1 monoclonal antibody and total-Cav1 polyclonal antibody. In parallel, cells were imaged using a PerkinElmer UltraView dual spinning-disk confocal microscope stage with 37°C stage and 100× objective. Recordings were initiated and followed after addition of 10 mg/ml BSA (albumin). Live-cell *z*-stacks were recorded (0.2-μm-step increments at 200-ms exposure time) for 20 min. Recorded data were analyzed by Volocity particle tracking software to determine the number (B), velocity (C), and volume (D) of mobile fluorescent vesicles (Cav1-GFP+). Values are displayed as percentile plots ± SD (left) or corresponding bar graph of median values ± SD (right) for each treatment. A nonparametric Kolmogorov–Smirnov test was used to compare the cumulative distribution between control and treated groups in percentile plots, and ANOVA was used to analyze values in the bar graphs; *$p < 0.05$ vs serum free; $n = 5$.

trafficking velocity (Figure 1C), although this was not statistically significant.

Characterization of phosphoY14-Cav1 mutants expressed in rat lung endothelial cells

To assess further the role of Cav1 phosphorylation on vesicle trafficking, we stably expressed WT, phosphomimicking Y14D, and phosphodefective Y14F mutants of Cav1 in RLMVECs by retroviral infection and G418 selection. Examination by EM indicated the presence of caveolae-like invaginations continuous with the plasma membrane, as well as of free-cytoplasmic vesicles, in cells expressing WT-Cav1 (Figure 2, A and B). Formation of both types of caveolae was ~30% greater per 100 μm of cell length in cells expressing the Y14D mutant (Figure 2B), suggesting that Y14D has a dominant-positive effect on caveolae formation relative to endogenous Cav1 in RLMVECs. We found exactly the opposite to be true for Y14F Cav1, as expression reduced vesicle number by 38% ($p < 0.05$), and thus Y14F acted as a dominant-negative mutant (Figure 2, A and B). We also measured uptake of radioactive ^{125}I-albumin in stably transfected RLMVECs and observed that the Y14F mutant reduced endocytosis of albumin by ~45%, whereas the phosphomimicking Y14D mutant increased ^{125}I-albumin uptake more than sevenfold compared with cells overexpressing WT-Cav1 (Figure 2C). Because Cav1 phosphorylation can affect Cav1 gene expression (Orlichenko *et al.*, 2006; Joshi *et al.*, 2012), we also measured expression levels of endogenous Cav1 and cavin-1/PTRF in RLMVECs stably expressing Myc-tagged Cav1 constructs, as shown in Figure 2D. We observed that the expression of Y14D, but not of WT-Cav1 or Y14F-Cav1, increased the expression of endogenous Cav1 and cavin-1/PTRF approximately fivefold. These data suggest that the observed increase in the number of caveolae measured by EM could be due to increased biogenesis of caveolae, as previously described (Joshi *et al.*, 2012; Orlichenko *et al.*, 2006), in addition to an acute effect of phosphorylation on vesicle formation and budding.

Using TIRF microscopy (Figure 3, A and B), we were able to directly observe and quantify the appearance and disappearance of Cav1-GFP–labeled vesicles within the evanescent field that included the basal membrane of endothelial cells (Supplemental Figure S2 Movie). The number of docking and detachment events increased 3.5 times in RLMVECs expressing the Y14D construct, whereas the number of events detected was significantly reduced (by 45%) in cells expressing the phosphorylation-defective Y14F mutant (Figure 3B). Quantification of the number of mobile vesicles indicated that Y14D-GFP+ vesicles were 40% more mobile, whereas Y14F-GFP+ vesicles were 40% less mobile (Figure 3C), compared with WT-Cav1-GFP–labeled vesicles. The number of mobile Y14F-GFP+ vesicles did not increase when RLMVECs were treated with medium containing fetal bovine serum (FBS; Figure 3C, striped bar). When temporally monitored by spinning-disk confocal microscopy, WT-Cav1-GFP objects tracked by Volocity software exhibited a 3D fluorescent volume of 0.153 ± 0.028 μm^3 moving at a speed of 0.175 ± 0.025 μm/s. The velocity and volume of Y14F-GFP+ vesicles was significantly reduced by 55% (Figure 3D) and 40% (Figure 3E), respectively, whereas the Y14D mutant formed vesicles that were 1.9 times larger but moved at the same speed as WT-Cav1+ vesicles (Figure 3, D and E).

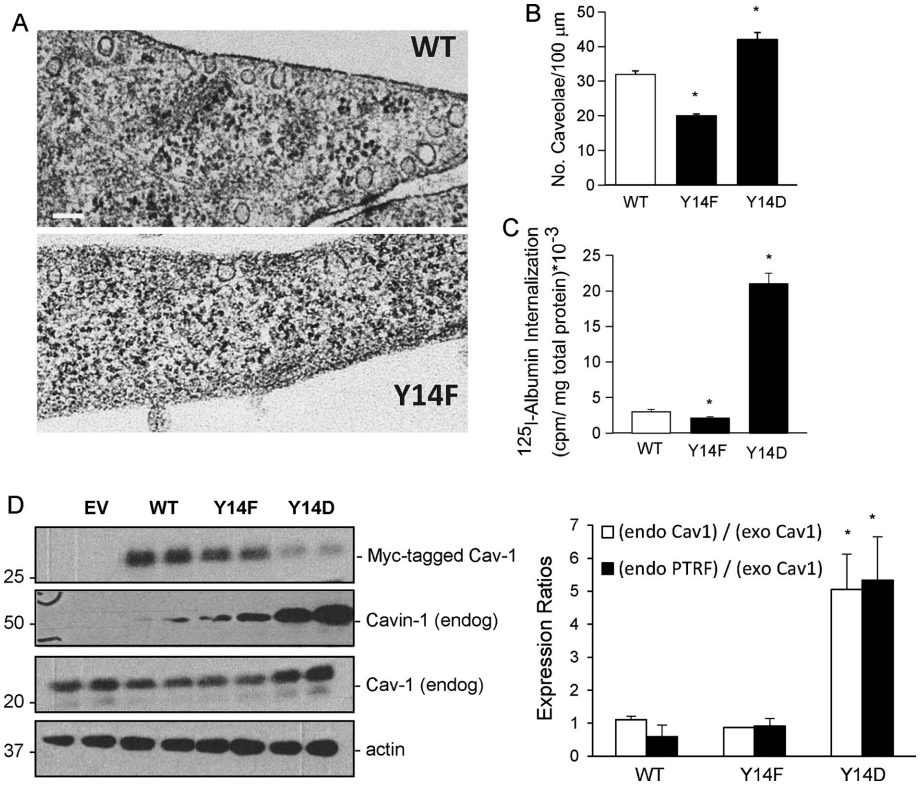

FIGURE 2: Phosphomimicking Cav1 Y14D mutant increases caveolae number and ^{125}I-albumin internalization in rat lung endothelial cells. RLMVECs were transfected by electroporation with GFP-tagged Cav1 constructs. (A) Representative electron micrographs juxtaposing images of cells transfected with WT-Cav1 and Y14F-Cav1 mutants; scale bar, 100 nm. (B) Bar graph summarizing the number of caveolae per 100 µm of cell length visualized by electron microscopy of thin sections of RLMVECs transfected with WT, Y14F, and Y14D Cav1 constructs (mean ± SD). (C) ^{125}I-albumin internalization in RLMVEC cells stably expressing WT, Y14F, and Y14D constructs of Cav1. Cells were plated in six-well plates, grown until confluent, and serum deprived for 2 h, and then specific uptake of ^{125}I-albumin was measured at 37°C for 20 min. ^{125}I-albumin counts per minute were normalized to the total cellular protein per well (*$p < 0.05$; $n = 3$). (D) Cell lysates of stably transfected RLMVEC cells expressing Myc-tagged WT-, Y14F-, or Y14D-Cav1 constructs were boiled and analyzed by Western blotting using total Cav1 pAb (BD Transduction Laboratories) or cavin-1 pAb (PTRF pAb; ProteinTech). Endogenous Cav1 and cavin-1 were detected at ~22 and ~50 kDa, respectively, whereas overexpressed Myc-tagged Cav1 constructs ran at ~25 kDa. The intensity of bands was analyzed by densitometery (ImageJ) and normalized to actin. Expression of endogenous Cav1 and cavin-1 were normalized relative to overexpressed Myc-Cav1 protein. *$p < 0.05$; $n = 3$.

WT Cav1 or Y14D Cav1 rescue albumin uptake in *Cav1*$^{-/-}$ mouse lung endothelial cells

We next assessed Cav1-GFP+ vesicle trafficking in mouse lung endothelial cells (MLECs) isolated from *Cav1*$^{-/-}$ mice to determine the effect of Cav1 phosphomutants on formation of caveolae and dynamics of albumin internalization. When tracked by spinning-disk confocal microscopy, the median velocity of Y14F-Cav1-GFP+ vesicles was 55% slower (0.13 ± 0.02 µm/s; $p < 0.05$) than WT-Cav1-GFP+ vesicles (0.3 ± 0.012 µm/s; $p < 0.05$; $n = 4$), whereas Y14D-GFP+ vesicles moved at a speed that was not significantly different from that for WT-Cav1 (Figure 4A). With respect to volume, the phosphodefective Y14F-Cav1 mutant formed vesicles that were ~30% smaller (0.11 ± 0.02 µm^3), and phosphomimicking Y14D mutant-generated vesicles that were 50% larger (0.3 ± 0.03 µm^3), than with WT-Cav1-GFP (Figure 4B).

To test the ability of the Cav1 Y14 mutants to rescue caveolae-mediated albumin uptake in *Cav1*$^{-/-}$ MLECs, we expressed Myc-tagged Cav1-constructs and assessed fluorescent albumin uptake in Myc-positive cells. Expression level of each of the constructs was equivalent, as detected by Western blotting with anti-Myc antibody under standard conditions (Figure 5A, left). Uptake assays were performed for 30 min at 37°C with Alexa 488–labeled BSA, followed by extensive washing to remove any surface-bound albumin (Figure 4C). The amount of internalized BSA in fixed cells was determined using confocal microscopy based on the fluorescence intensity of Alexa 488, and localization of Myc-tagged WT, Y14F, and Y14D Cav1 proteins was visualized with anti-Myc primary and Alexa 568 secondary antibodies (Figure 4C). Myc staining in cells expressing WT-Cav1 or Y14D-Cav1 mutant was observed at the plasma membrane and in cytoplasmic vesicles, the latter being more pronounced with the Y14D mutant (Figure 4C). In contrast, Y14F-Cav1 expression was limited primarily to the plasma membrane. The Alexa 488 signal indicated that BSA was internalized and colocalized with Myc staining in WT-Cav1– and Y14D-Cav1–transfected cells but not in cells expressing Y14F-Cav1, in which internalized Alexa 488 fluorescence was minimal. We conclude that phosphorylation-competent WT Cav1 and phosphomimicking Y14D Cav1 mutants, but not Y14F Cav1, can rescue albumin uptake in *Cav1*$^{-/-}$ MLEC cells.

Y14D Cav1 mutant dissociates readily into monomers and enters the cytosolic fraction in nonboiled samples

Depending on the method of sample preparation and running conditions for Western blots, Cav1 runs exclusively as a monomeric species of ~22 kDa when boiled in standard sample buffer or as a combination of monomers and high-order molecular species (>250 kDa) when the reducing agent and/or boiling is omitted (Kurzchalia *et al.*, 1992; Li *et al.*, 2001). In agreement, we observed that boiled lysates prepared from *Cav1*$^{-/-}$ MLECs transfected with Myc-tagged constructs of WT-Cav1, Y14D, and Y14F Cav1-mutants all ran as a single band of 25 kDa (3 kDa Myc + 22 kDa Cav1), confirming equal expression and loading in each lane (Figure 5A, left). However, when the same samples were analyzed without boiling (60°C for 10 min), they appeared as bands at 25 and >250 kDa, the distribution of which depended on the charge of the residue at position 14 in each construct. The band at >250 kDa was most pronounced for the WT and phosphodefective Y14F mutant but barely detectable for phosphomimicking Y14D-Cav1, which ran as a 25-kDa monomeric band (Figure 5A, right). As a control, we expressed the C156S Cav1 construct and showed that in nonboiled samples it too runs predominantly as a monomer, consistent with our previous observation (Bakhshi *et al.*, 2013).

To explore the effect of phosphorylation on oligomerization of Cav1, we transduced HEK cells with Myc-tagged Cav1 constructs and performed subcellular fractionation in 5–30% sucrose gradients

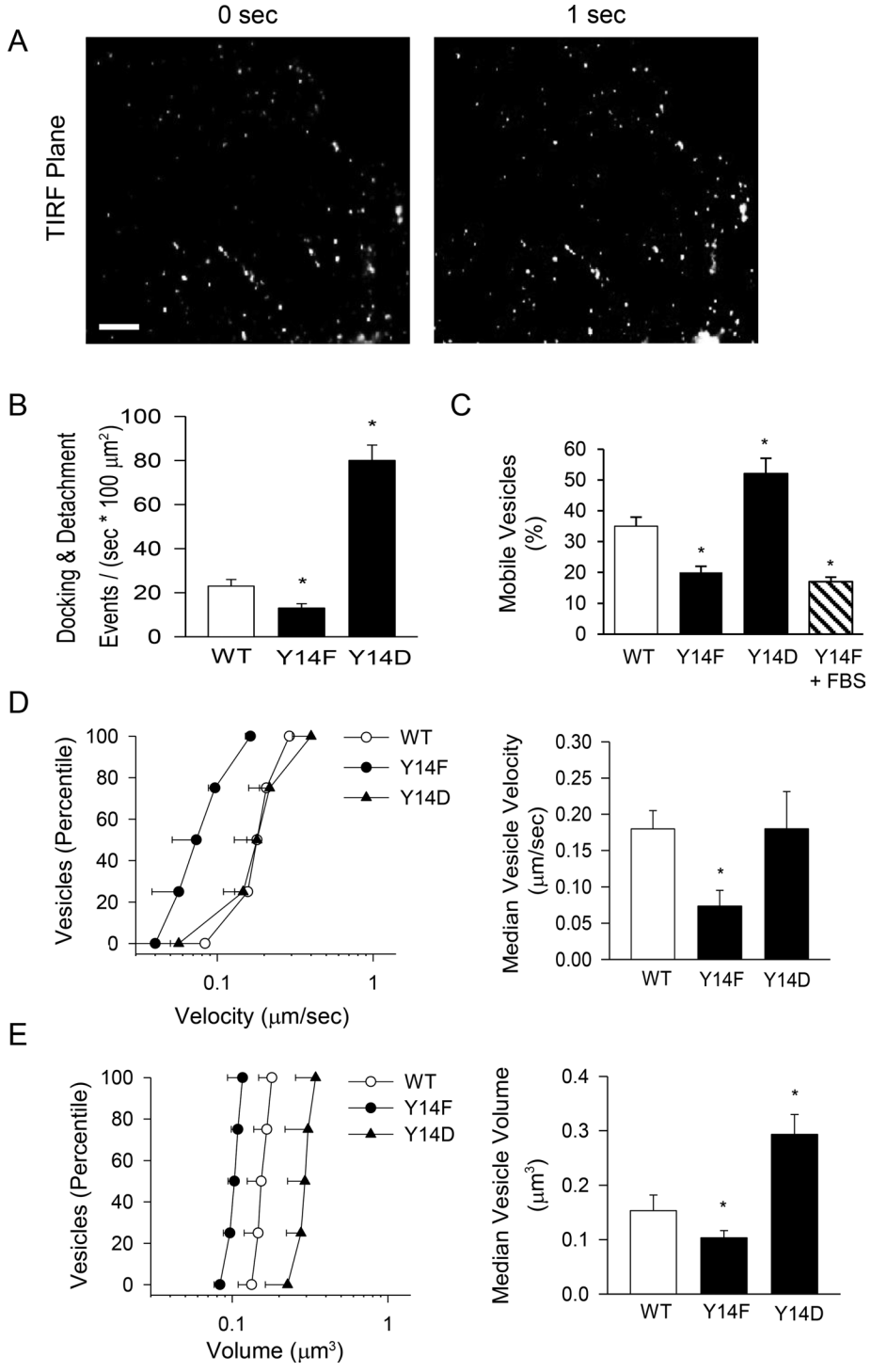

FIGURE 3: Phosphomimicking Y14D-Cav1-GFP mutant increases vesicle number, volume, and docking/detachment events. RLMVECs were transfected by electroporation with GFP-tagged Cav1 constructs, including WT, Y14F, and Y14D. (A) TIRF microscopy (frame rate of acquisition at 1 frame/s) shows two consecutive frames depicting the GFP-labeled Cav1-WT vesicles in the TIRF plane (<200 nm from the glass surface) near the basal membrane; scale bar, 2 μm. (B) Summary of the number of docking/detachment events of Cav1-GFP fluorescent vesicles in the TIRF plane, estimated by subtracting each frame from the previous one using the Delta F-up ImageJ module; $n = 5$. (C–E) Spinning-disk confocal microscopy and Volocity particle tracking analysis. (C) Percentage of mobile Cav1 WT-GFP+, Y14D-GFP+, and Y14F-GFP+ vesicles in serum-deprived cells, calculated by dividing the number of mobile fluorescent objects by the total number of fluorescent objects. Striped bar depicts Y14F mutant in the presence of added FBS. (D, E) Percentile plots and bar graphs of median velocity (D) and volume (E) obtained for WT, Y14F, and Y14D-Cav1-GFP mutants. Experiments were performed at least in triplicate and statistical comparison between the constructs determined by ANOVA; *$p < 0.05$.

followed by sample preparation in mild detergent (2% *n*-octyl-β-D-glucopyranoside [ODG]) and low heat (60°C). In the 11 fractions collected starting from the top and loaded on the gel in sequence, we observed a clear overall shift toward monomeric bands for the Y14D mutant (Figure 5D) and an opposite shift toward oligomeric bands for the Y14F mutant (Figure 5C), whereas WT-Cav1 distributed more evenly (Figure 5B).

When clarified lysates from HEK cells transfected with Myc-tagged Cav1 constructs were subjected to ultracentrifugation in order to isolate membrane and cytosolic fractions and therefore roughly separate PM-associated Cav1 from the cytosolic Cav1+ vesicles, we observed that Myc-tagged WT-Cav1 and the Y14F mutant were localized in the membrane fraction and ran predominantly as high–molecular weight oligomers (>250 kDa; Figure 5E, right). In contrast, the Y14D mutant ran mostly as a 25-kDa monomer and appeared in both the cytosolic and membrane fractions (Figure 5D), thus following a similar subcellular distribution as the C156S mutant, which was previously reported to be hyperphosphorylated at Y14 (Bakhshi *et al.*, 2013). These results suggested to us that 1) a shift in the distribution of Cav1-positive vesicles from the PM to the cytosol is associated with modification of Cav1 molecules that makes Cav1 oligomers less stable in SDS, and 2) Y14 phosphorylation, as mimicked by the Y14D mutant, facilitates destabilization of Cav1 oligomers in the caveolar coat.

Phosphorylation of endogenous Cav1 leads to dissociation of higher-order Cav1 oligomers

To confirm that the destabilization of Cav1 oligomers induced by phosphorylation is not an artifact of overexpression of mutant proteins (i.e., also occurs with endogenous Cav1 protein present in endothelial cells), we treated RLMVECs with 25 μM Na_3VO_4 for 30 min and examined the monomer-to-oligomer profile of endogenous Cav1 in the fractions collected from 5–30% sucrose gradients. As shown in Figure 6A, we observed a shift in Cav1 distribution toward the 22-kDa species when RLMVECs were treated with a tyrosine phosphatase inhibitor, Na_3VO_4; we observed a similar trend when serum-deprived human lung

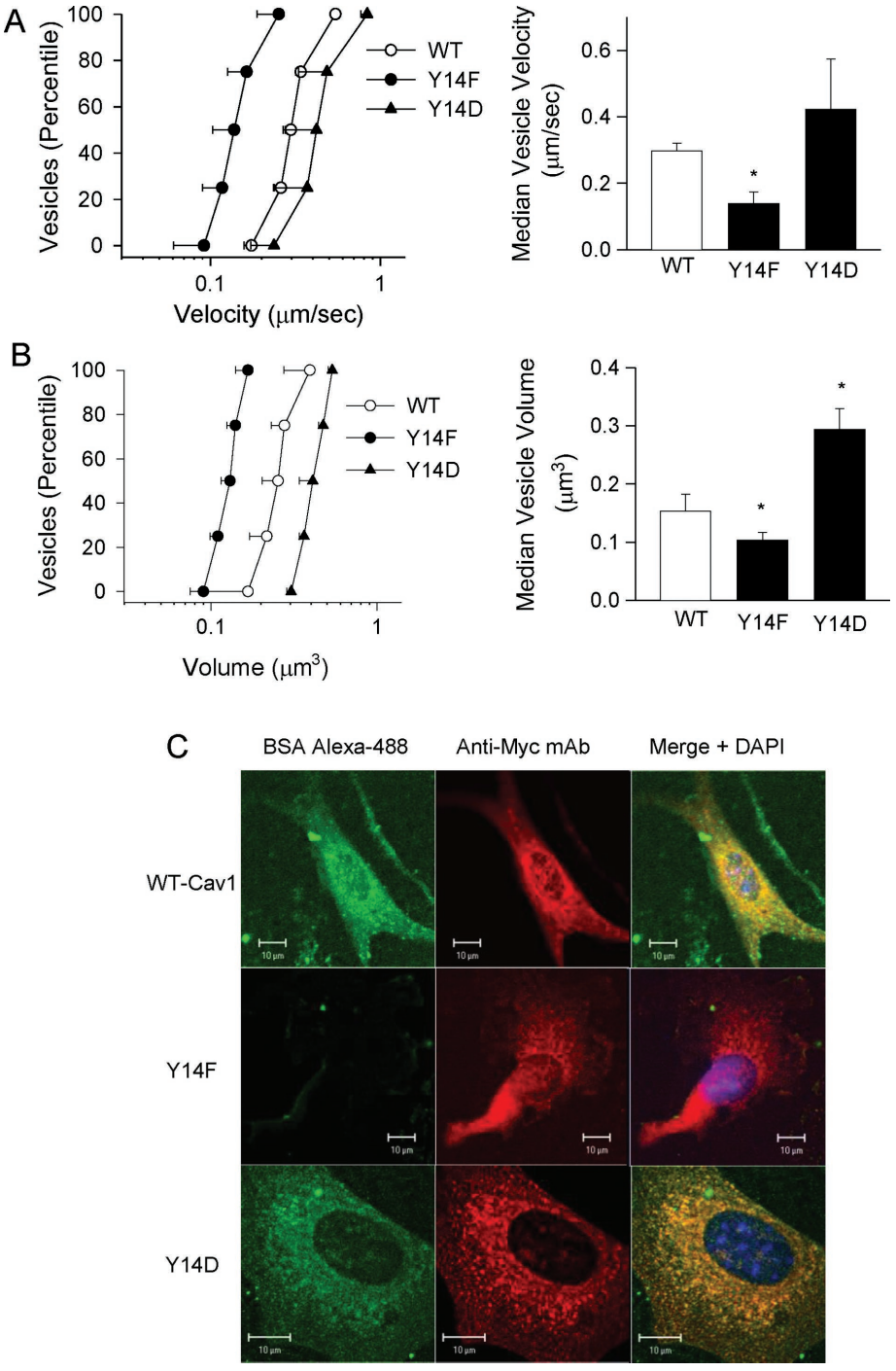

FIGURE 4: Phosphomimicking Cav1 Y14D mutant increases vesicle volume and rescues BSA-uptake in Cav1-null mouse lung endothelial cells (Cav1$^{-/-}$ MLECs). GFP-tagged WT- and Y14-Cav1 point mutant were transfected by electroporation into Cav1$^{-/-}$ MLECs isolated from *Cav1*$^{-/-}$ lungs (see *Materials and Methods*) and examined by dual spinning-disk confocal microscopy. Velocity (A) and volume (B) of tracked mobile vesicles was determined using Volocity particle-tracking software and plotted as percentile plots (left) and bar graphs of median values ± SD (right). Experiments were performed in triplicate and statistically analyzed by ANOVA. *Significant difference compared with WT ($p < 0.05$). (C) Alexa 488–BSA uptake visualized by confocal microscopy in *Cav1*$^{-/-}$ MLECs transfected with Myc-tagged Cav1-constructs, including WT, Y14F, and Y14D. Cells were incubated with 0.1 mg/ml Alexa 488–labeled BSA plus 1 mg/ml unlabeled BSA for 30 min at 37°C, placed on ice, and then extensively washed with ice-cold acid wash buffer and PBS. Cells were fixed and probed with anti-Myc primary Ab, followed by Alexa 568–conjugated secondary Ab to visualize Cav1, in conjunction with internalized Alexa 488–tagged BSA. Images are representative of four separate experiments.

microvascular endothelial cells (HLMVECs) were stimulated with BSA in the presence of Na_3VO_4 (Figure 6B). When the blot in Figure 6A was stripped and reprobed with anti-pY14 Cav1 monoclonal Ab (mAb; Supplemental Figure S3), only monomers were detected; the 75-kDa band was previously shown to be pY-paxillin (Hill *et al.*, 2007). Consistent with our hypothesis that oligomer stability is modified by phosphorylation, treatment of HLMVECs with BSA in the presence of Na_3VO_4 (V, lane 2) increased Y14 phosphorylation 1.5 times and the monomer/oligomer ratio 2-fold. Not surprisingly, treatment with Src-family kinase inhibitor PP2 blocked BSA/Na_3VO_4-dependent Y14-Cav1 phosphorylation and monomer formation (Figure 6B, lane 3).

RapR-Src activation by rapamycin leads to Cav1 oligomer destabilization, whereas Src inhibition by antennapedia–caveolin-1 scaffold domain stabilizes oligomers of Cav1

We next used recombinant c-Src protein engineered to be rapidly and specifically activated inside the cell upon addition of rapamycin. The rapamycin-regulated activatable Src system (RapR-Src) consists of an inhibitory FRB domain that can be quickly removed by rapamycin to disinhibit RapR-Src activity (Chu *et al.*, 2014). To test the effect of Src activation on endogenous Cav1 phosphorylation and oligomerization, we infected HLMVECs with viral supernatants of FRB and RapR-Src expression constructs for 24 h and then serum deprived them for 4 h. To assess the effect of RapR-Src on distribution of Cav1 oligomers, we treated cells with 0.5 μM rapamycin or vehicle for 5–60 min and assessed them by Western blot. The distribution of Cav1 monomers/oligomers in nonboiled lysates indicated that within 10 min after addition of rapamycin, there was an increase in Cav1 phosphorylation and a corresponding and proportional appearance of 22-kDa Cav1 protein at the expense of higher–molecular weight (>250 kDa) Cav1 oligomers (Figure 7, A and B). As a positive control for RapR-Src activation, we probed for phosphorylated Y118-paxilin, a well-characterized downstream substrate of Src, which we also observed to be rapidly phosphorylated and to remain so throughout the entire time course.

In a similar but opposite manner, we used the caveolin scaffold domain (CSD) peptide (amino acids 82–101) conjugated to the antennapedia protein transduction domain (Antp; Bucci *et al.*, 2000) to block Src activation, presumably by direct

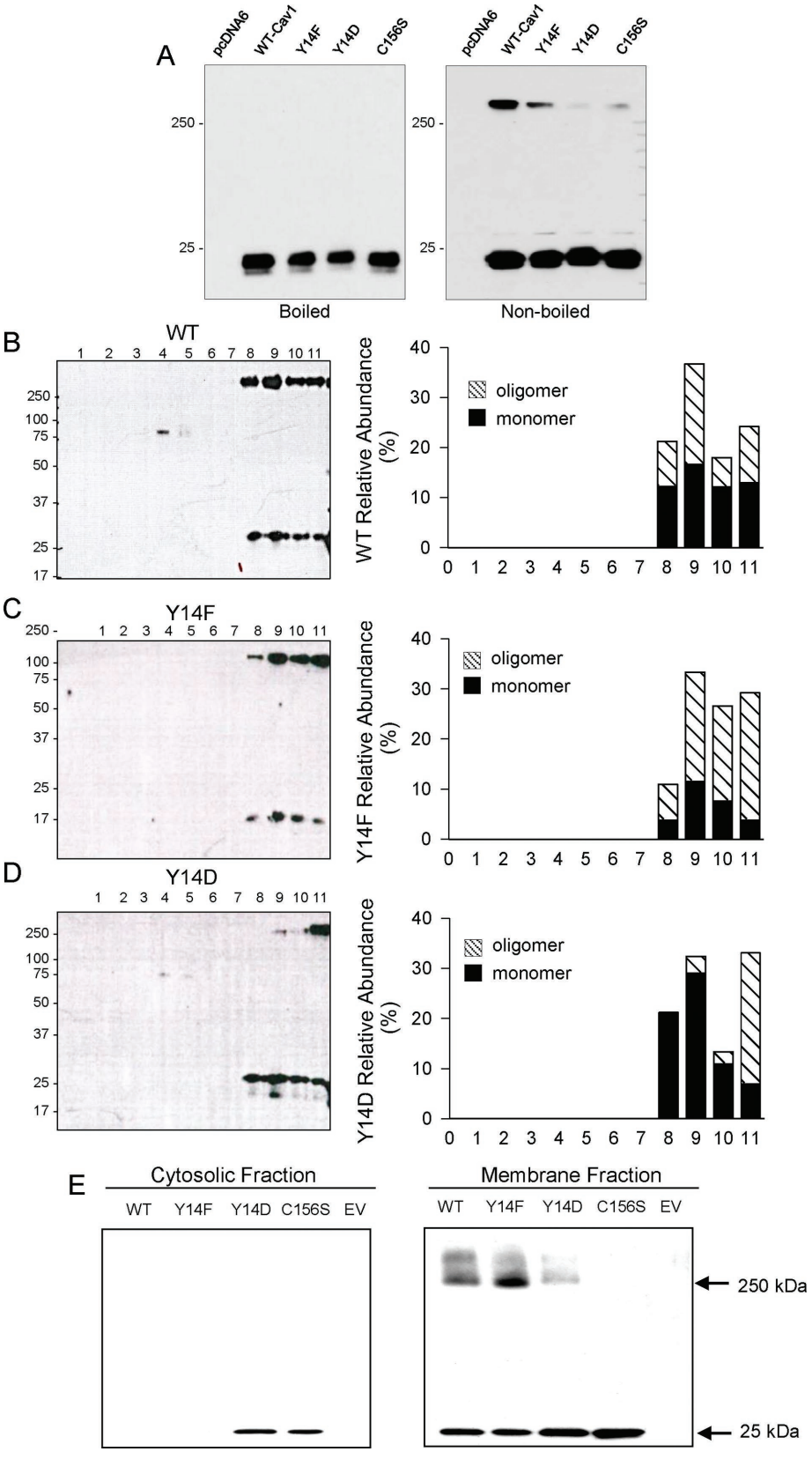

FIGURE 5: Y14D mutant readily dissociates into monomers in nonboiled samples, shifts the distribution toward monomers on sucrose gradients, and partitions into the cytosolic fraction. (A) Western blot analysis of boiled and nonboiled lysates of Myc-tagged Cav1 constructs in *Cav1*$^{-/-}$ MLECs. To detect *Cav1*$^{-/-}$ MLECs expressing WT-Cav1, Y14F, Y14D and C156S mutants were lysed and blotted using standard conditions (including RIPA buffer and boiling) or gently solubilized in saline buffer supplemented with 2% ODG and heated at 60°C to preserve higher-order oligomers ("nonboiled"). Membranes were blotted with anti-Cav1 pAb. HEK cells expressing (B) WT-Cav1, (C) Y14F-Cav1, or (D) Y14D-Cav1 were fractionated by density gradient centrifugation on 5–30% sucrose gradients. Eleven equal fractions, with the top fraction (1) being the lightest and bottom fraction (11) the heaviest, were analyzed by Western blot using anti–total Cav1 pAb. Bar graphs depicting the distribution (relative abundance) of Cav1 oligomers and monomers in each lane were calculated as a percentage of the total Cav1 in the entire blot. (E) Analysis of cytosolic and total membrane fractions from *Cav1*$^{-/-}$ MLECs expressing Myc-tagged Cav1 cDNAs. Detergent-free cell homogenates were clarified by low-speed spin (500 × *g*) to remove nuclei and unbroken cells, and then supernatants were ultracentrifuged at 55,000 rpm in a TLA-55 Beckman rotor to separate supernatant (cytosol/microvesicle fraction) from the pelleted total membrane fraction (pellet). The two fractions were then solubilized and adjusted to the same concentration, heated in sample buffer at 60°C ("nonboiled"), and resolved on SDS–PAGE gels, followed by detection with anti–total Cav1 pAb. The C156S Cav1 mutant was used as a negative control for Cav1 oligomerization (Bakhshi *et al.*, 2013).

binding (Li *et al.*, 1996a; Okamoto *et al.*, 1998). As shown in Figure 7C, addition of 5 μM Antp-CSD to RLMVECs blocked albumin-induced Y418 Src and Y14 Cav1 phosphorylation (Figure 7C). Separation of Antp-CSD–treated RLMVEC homogenates into cytosolic and membrane fractions revealed a reduction in the 22-kDa Cav1 monomer band in the soluble fraction (Figure 7D) and a corresponding increase in the high–molecular weight Cav1 oligomer band (>250 kDa) in the membrane fraction as compared with Antp alone. To corroborate these results, we also observed that transcytosis of ^{125}I-albumin across confluent monolayers of RLMVECs cultured on porous Transwell inserts was reduced in cells treated with Antp-CSD (Figure 7E).

Acceptor-photobleaching FRET efficiency and coimmunoprecipitation indicate decreased interaction between Y14D-Cav1 monomers in the caveolar coat

Our data thus far indicate that Cav1-Y14 phosphorylation triggers volume expansion and internalization/trafficking of Cav1-positive vesicles in live cells, as observed by confocal and TIRF microscopy, and a corresponding destabilization of Cav1

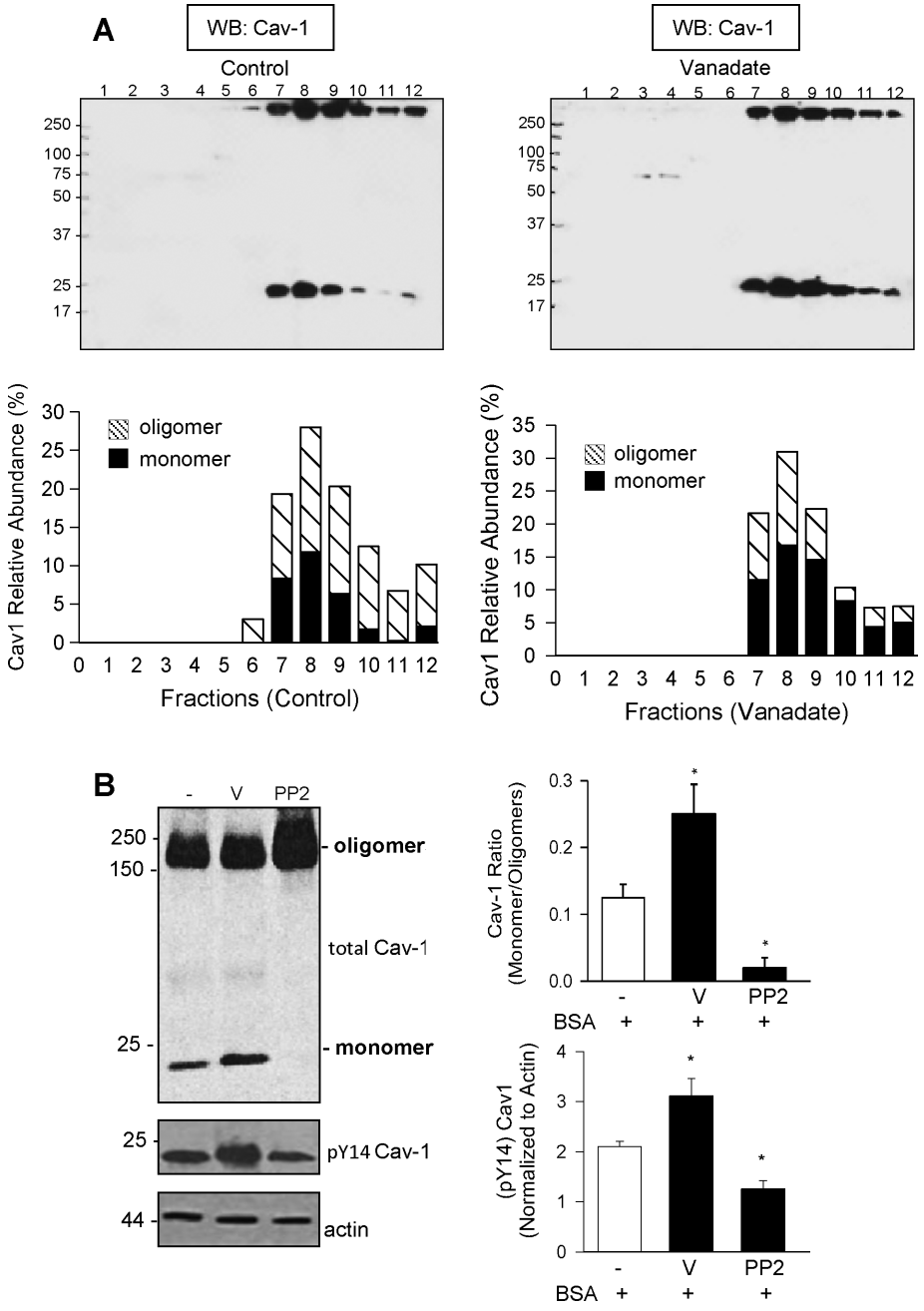

FIGURE 6: Endogenous Cav1 oligomers are readily destabilized in the presence of phosphatase inhibitor in nonboiled rat lung and human lung endothelial cells. (A) Endogenous Cav1 monomer-to-oligomer distribution (relative abundance) in RLMVEC lysate fractions collected from 5–30% sucrose gradients indicates that there is a shift toward the 22-kDa monomeric species after treatment with 100 μM Na_3VO_4 for 30 min. Twelve equal fractions were collected from the top, with fraction 1 being the lightest and fraction number 12 the heaviest. The bar graph depicts the relative abundance of Cav1 oligomers and monomers in each lane (striped bar vs. solid black) as a percentage of total Cav1 on each Western blot. (B) Western blot analysis of endogenous Cav1 in nonboiled HLMVEC lysates. Appearance of the 22-kDa Cav1 monomer at the expense of high–molecular weight Cav1 oligomers in endothelial cells treated with 3 mg/ml albumin was significantly enhanced in the presence of the phosphatase inhibitor,Na_3VO_4 (V, lane 2) and reduced in presence of Src inhibitor PP2 (lane 3). Boiling the samples to detect phospho-Cav1 indicated that there was corresponding phosphorylation of Cav1 Tyr-14, and reprobing the same blot for actin indicated equal loading of all lanes. *$p < 0.05$; $n = 3$.

oligomers, as observed biochemically by Western blotting. These data suggest that Cav1 phosphorylation may lead to expansion and release of caveolae from the plasma membrane by weakening the physical forces that maintain the oligomeric Cav1 inner membrane coating and should be detectable as spatial separation, or distancing, between individual Cav1 molecules. To test this prediction, we measured FRET between fluorescent Cav1 acceptor/donor pairs cotransfected in HEK cells. Using a combination of yellow fluorescent protein (YFP)– and cyan fluorescent protein (CFP)–tagged Cav1 constructs, we assessed FRET efficiency before and after photobleaching the acceptor (YFP) with the 514-nm laser, as shown in the representative image of WT-Cav1 (Figure 8A). FRET efficiency for each YFP/CFP pair of Cav1 proteins in fixed HEK cells was calculated from confocal images excited at 458 nm before and after photobleaching with the 514-nm laser (regions of interest [ROIs] for the FRET analysis were situated in peripheral regions of the cell). The greater the increase in the observed intensity of donor (CFP) after bleaching of the acceptor (YFP), the greater is the FRET efficiency and the closer is the association within the CFP/YFP pair. As quantified in Figure 8B, we observed significantly greater FRET efficiency for the Y14F mutant (0.90 ± 0.13) than the Y14D mutant (0.21 ± 0.08), suggesting that Y14F-Cav1 molecules form closer connections within the scaffold.

We also tested the strength of self-association between Cav1 monomers in the caveolar coat by coimmunoprecipitation. HEK cells expressing Myc-tagged WT-Cav1 were cotransfected with either CFP-tagged WT-Cav1 or CFP-tagged Y14D mutant. The pull down of Myc-tagged Cav-1 was accomplished with anti-Myc polyclonal antibody (pAb; Abcam, Cambridge, MA), and coimmunoprecipitated CFP-tagged Cav1 was measured in boiled samples with anti-Cav1 mAb by Western blotting. Because the CFP-tagged Cav1 monomer runs at 53 kDa and Myc-tagged Cav1 monomer appears at 25 kDa, the efficiency of coimmunoprecipitation expressed as the ratio of 53/25-kDa band intensities (i.e., the ratio of CFP/Myc) and normalized to the pre-immunoprecipitation expression levels for each construct (inputs) was used to assess their interaction in situ. As summarized in Figure 8C (right), Myc-tagged wild-type Cav1 coimmunoprecipitation was twofold greater with CFP-tagged WT Cav1 than with the CFP-tagged Y14D mutant, suggesting that Cav1 phosphorylation weakens Cav1/Cav1 interactions.

Live-cell FRET imaging to gauge spatial distribution of Cav1 monomers upon phosphorylation

To visualize the dynamic alterations in spatial arrangement of Cav1 molecules in the caveolar coat during Cav1 phosphorylation and

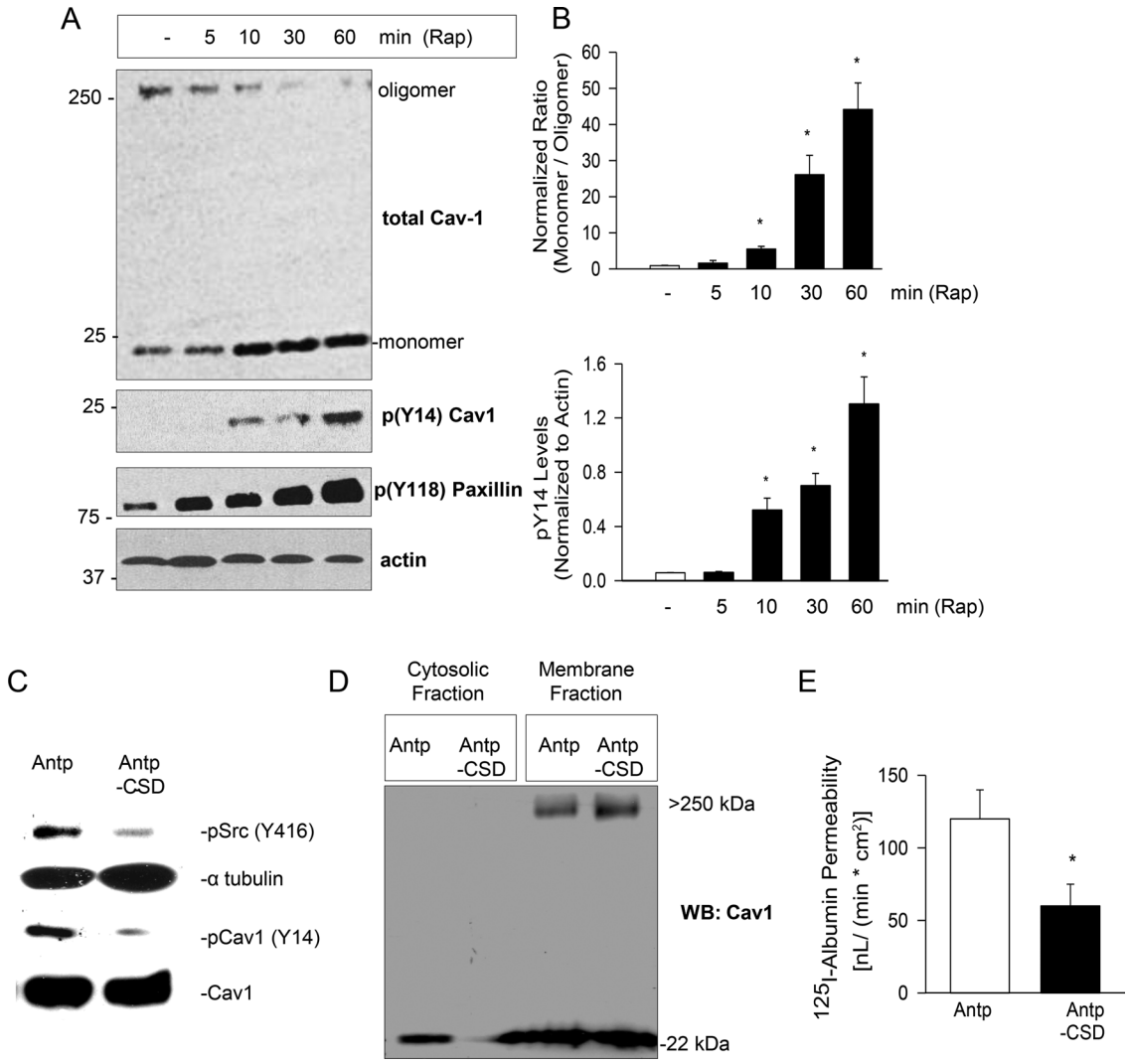

FIGURE 7: Activation of engineered RapR-Src leads to rapid destabilization of Cav1 oligomers, whereas inhibition of Src by Antp-CSD stabilizes Cav1 oligomers in the membrane fraction. (A) HLMVECs were infected for 24 h with viral supernatants carrying FRB and RapR-Src expression constructs. The cells were then serum starved and either left untreated (0 min rapamycin) or treated with rapamycin for 5–60 min to activate RapR-Src. Changes in endogenous Cav1 phosphorylation and distribution of Cav1 monomers and oligomers (monomer/oligomer ratio) with time were monitored by Western blotting using anti-Cav1 pAb, phospho-Y14 Cav1 mAb, and actin (loading control). Phospho-Y118 paxillin (pAb) was used as a positive control for RapR-Src activation. (B) Bar graphs depicting the inverse ratio of Cav1 monomers to oligomers (top) and the level of pY14 Cav1 normalized to actin (bottom); intensities of Western blot bands are shown as mean ± SD ($n = 3$, $^*p < 0.05$). (C–E) Cell-permeant peptide (Antp, negative control) or Antp-conjugated to the Cav1 scaffold domain peptide (Antp-CSD), both at 5 μM, were applied to RLMVECs for 1 h at 37°C. (C) Western blot indicates that Antp-CSD inhibits Src activity, as determined by the decrease in phosphorylation level of Src-Y416 and Y14-Cav1, the downstream target of Src. (D) Lysates from cells treated with Antp or Antp-CSD were subject to ultracentrifugation (55,000 rpm) to separate cytosolic from membrane fractions (pellet). Western blotting revealed that in cells treated with Antp-CSD, there is a loss of the 22-kDa Cav1 monomeric band from the cytosolic fraction (lane 2) and a corresponding appearance of a stronger Cav1 band in the membrane fraction (lane 4) at high molecular weight (>250 kDa). (E) ^{125}I-albumin transcytosis across confluent monolayers of RLMVECs loaded with 5 μM Antp-CSD is inhibited in comparison to cells loaded with 5 μM Antp ($^*p < 0.05$; $n = 3$).

activation of endocytosis, we measured FRET continuously in live HEK cells before and after stimulation with 3 mg/ml BSA. HEK cells were cotransfected with YFP- and CFP-conjugated Cav1 cDNA FRET donor/acceptor pairs. After 24 h, cells were serum deprived for 2 h and moved to a heated stage in an environmentally controlled chamber of Zeiss LSM 710 microscope equipped with GaAsP detector (Zeiss, Jena, Germany). Cells that expressed equal levels of CFP and YFP constructs were chosen for subsequent FRET measurements (Figure 9A*b*). FRET was recorded every 2 s from the Cav1+ vesicle pool throughout the plasma membrane and cytoplasm (Supplemental Figure S4, A–C, Movie) and normalized to the total CFP fluorescence at each time point. As shown in Figure 9A, we were able to detect a FRET signal in unstimulated HEK cells, indicating that the Cav1-YFP/Cav-1-CFP molecules incorporated in vesicles were in close proximity (<10 nm) and depended on the presence of Cav1, as cells transfected with CFP- and YFP-empty vectors did not produce a FRET signal (unpublished data). On BSA stimulation, we observed a gradual and steady

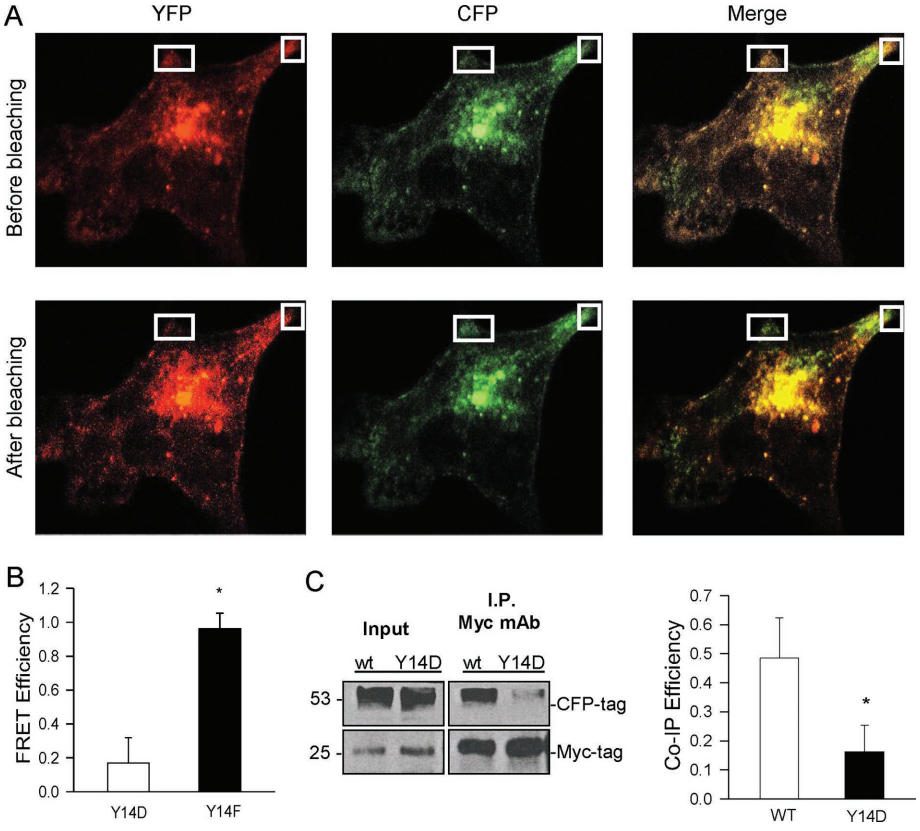

FIGURE 8: Interaction between Cav1 molecules in oligomerized caveolar coat measured by FRET efficiency and coimmunoprecipitation. (A, B) HEK cells coexpressing CFP- and YFP-tagged constructs of WT or Y14D-Cav1 were serum deprived, fixed, and examined by confocal microscopy. FRET intensity was measured using a 458-nm laser beam before and after photobleaching of the acceptor (YFP) in ROIs (white box) using a high-intensity 514-nm laser. (A) Representative images depicting an increase in donor intensity (green) after bleach of acceptor (red) within the ROI (white boxes) in WT-Cav1–expressing HEK cells. Note that donor and acceptor intensities did not change significantly in areas not subjected to photobleaching (outside the white box). (B) Bar graph summary of the FRET efficiency of Y14D and Y14F mutants, calculated from the fluorescence intensity of the donor (D) in the presence (I_{AD}) and absence (I_D) of the acceptor, that is, before and after photobleaching with a 514-nm laser: $E_{FRET} = (I_D - I_{AD})/I_D$. Values shown are mean ± SD ($n = 5$; *$p < 0.05$). (C) Coimmunoprecipitation of Myc-tagged WT-Cav1 cotransfected in HEK cells with either CFP-tagged WT-Cav1 or CFP-tagged Y14D mutant. Immunoprecipitation (I.P.) was by anti-Myc mAb and detection in boiled samples by Western blot using anti-Cav1 pAb. Myc-tagged Cav1 monomers run as 25-kDa bands and CFP-tagged ones as 53-kDa bands. Bar graph of coimmunoprecipitation efficiency expressed as a ratio of 53- over 25-kDa bands (corrected for the expression levels of each construct in the cell lysates, i.e., input). Values are mean ± SD ($n = 3$; *$p < 0.05$).

decrease in FRET (Cav1-YFP/Cav-1-CFP signal) and an increase in CFP fluorescence (dequenching) to ~70% of the initial value within 5–10 min (Figure 9A), consistent with the hypothesis that the "packing" of the oligomeric Cav1 coat changes during the process of albumin endocytosis. No significant changes in FRET were observed when either the Y14D or Y14F mutant was stimulated with BSA (Figure 9A and Supplemental Figure S4, B and C, Movie) indicating that these irreversible mutants did not undergo further FRET-sensitive conformational changes upon addition of BSA. We also measured changes in FRET in the presence and absence of the Src inhibitor PP2 and phosphatase inhibitor Na_3VO_4. Stimulation of cells with BSA in the presence of Na_3VO_4 induced a more dramatic decrease in FRET, whereas PP2 prevented any changes in FRET (Supplemental Figure S5).

When the same images were analyzed using Imaris fluorescent object counting software (Figure 9B and Supplemental Figure S4 Movies), we measured a threefold increase in the number of WT-Cav1+ vesicles upon BSA stimulation, coincident with the drop in FRET/CFP signal (Figure 9A). In contrast to WT-Cav1, the number of vesicles in Y14D-expressing cells did not change, that is, it remained high for the entire duration of the recording (see trace, Figure 9B, left). The number of vesicles in Y14F-Cav1–transfected cells was comparable to that of WT-Cav1–expressing cells at the onset of the experiment. However, in HEK cells expressing the Y14F mutant, there was no increase in vesicle count over time after addition of BSA, as summarized in the bar graph (Figure 9B, right, and Supplemental Figure S4C).

In a similar FRET experiment, HEK cells expressing YFP- and CFP-conjugated pairs of WT or Y14F Cav1 constructs were additionally cotransfected with FRB/RapR-Src cDNAs and real-time changes in FRET intensity measured before and after treatment with 0.5 μM rapamycin (Figure 9, C and D). Three minutes after rapamycin addition, a decrease in FRET intensity was observed (Figure 9C), which coincided with an increase in cytoplasmic fluorescent vesicle count for WT-Cav1 (Figure 9D), further supporting the inverse relationship between packing of Cav1 oligomers and internalization of Cav1+ vesicles.

To make sure that the measured changes in FRET ratio were real and not an artifact of local fluctuations in pH, we repeated experiments with WT-Cav1 conjugated with yellow fluorescent protein for energy transfer (YPET) in place of enhanced YFP (EYFP) and cyan fluorescent protein for energy transfer (CyPET) in place of enhanced CFP (ECFP; Supplemental Figure S6). Images were generated with the 458-nm laser line spanning an emission wavelength from 463 to 516 nm for detection of CyPET and from 526 to 608 nm for detection of YPET (FRET) in optical sections of <3.3 μm. We observed the same trend, that is, a steady decrease in YPET/CyPET ratio with time upon stimulation of cells with BSA, as observed with the EYFP/ECFP FRET pairs (Figure 9A). As expected, the decrease in FRET induced by BSA was completely abolished in the presence of PP2 (Supplemental Figure S6).

DISCUSSION

In this study, we show that phosphorylation-dependent molecular modification to the oligomerized caveolar coat evokes a biophysical change associated with an increase in trafficking of Cav1-GFP–positive vesicles. We assessed the contribution of Src-mediated phosphorylation of Y14 Cav1 using several approaches, including Cav1 overexpression in RLMVEC and HEK cells, Cav1 rescue of *Cav1*$^{-/-}$ MLECs, and phosphorylation of endogenous Cav1 protein in primary cultures of HLMVECs and RLMVECs. Regardless of the system used, we observed a strong correlation between Cav1 phosphorylation, destabilization of Cav1 oligomers, and increased velocity and

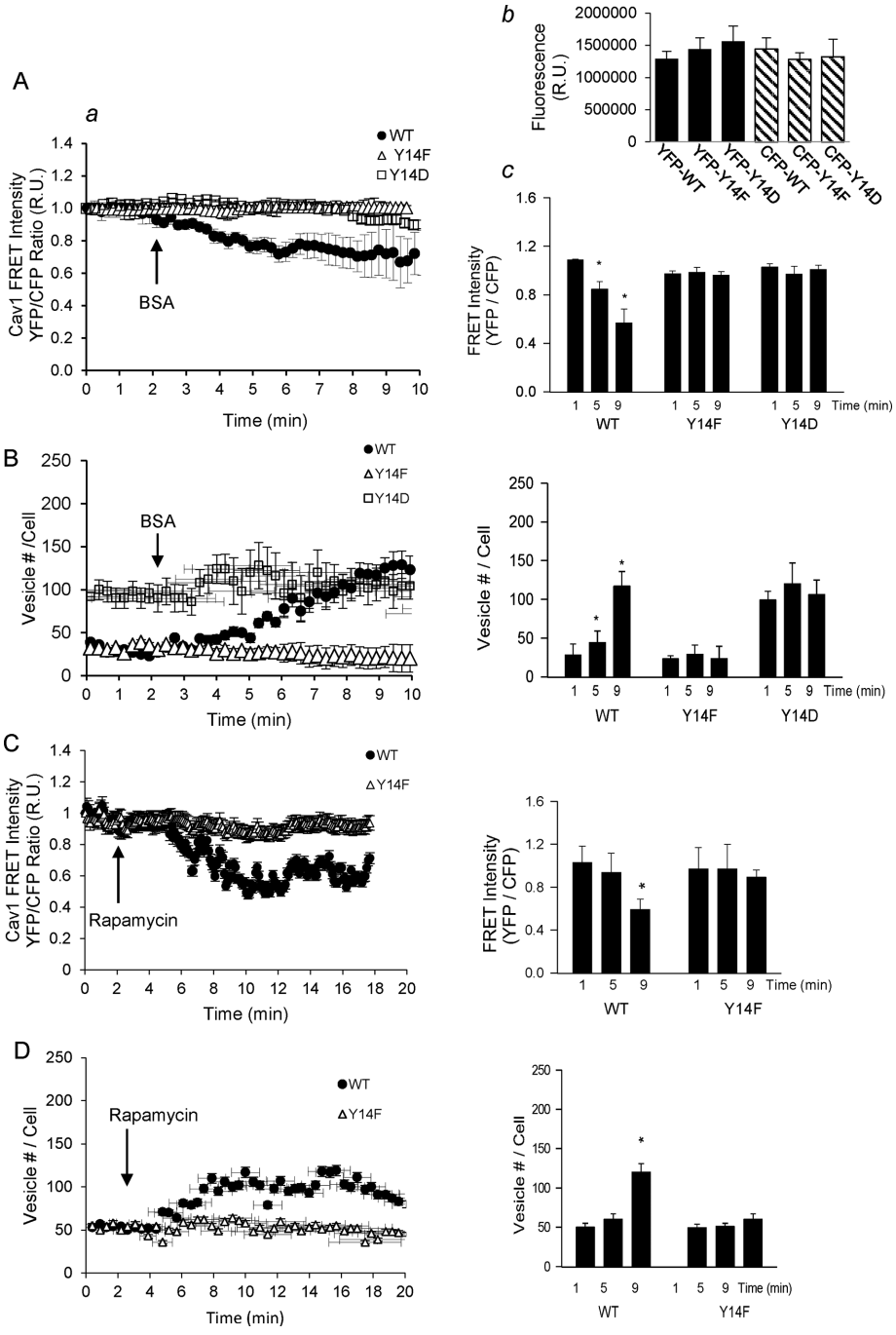

FIGURE 9: Dynamic changes in caveolin-1 during endocytosis of albumin monitored in real time by FRET. HEK cells were cotransfected with Cav1-YFP and Cav1-CFP constructs to create FRET pairs; empty CFP- and YFP-expression vectors were cotransfected as negative controls. At 24 h posttransfection, cells were serum deprived, and images were acquired with a Zeiss 710 BIG confocal microscope in a temperature- and CO_2/humidity-controlled chamber. FRET was recorded every 2 s using the 485-nm laser line for excitation; the 525- to 608-nm emission range was measured for FRET (YFP) and the 463- to 516-nm emission range for CFP, recorded as an internal control. After temperature equilibration and stabilization of fluorescence, recordings began, and basal FRET was collected for 2–5 min before stimulation with 3 mg/mL BSA, after which FRET was collected for an additional 20 min. At each time point, the FRET index was calculated (FRET/CFP) to account for temporal fluctuations in fluorescence. The FRET index before BSA stimulation (basal) was normalized to 1, and all subsequent time points were expressed as a fraction of the basal fluorescence. After data collection, ImageJ and Imaris software were used to analyze fluorescence intensity and count fluorescent objects at each time point. (A) (*a*) Trace showing the FRET/CFP fluorescence recording with respect to time, before and after BSA addition. (*b*) Expression levels of CFP- and YFP-tagged constructs per cell determined before FRET. (c) Bar graph summary of average FRET indices at 1, 5, and 9 min into the experiment for WT, Y14F, and Y14D-Cav1. (B) Left, number of fluorescent vesicles at each time point, before and after BSA stimulation. Right, bar graph summary of the number of vesicles at 1, 5, and 9 min into the experiment for WT, Y14F, and Y14D-Cav1. Data are mean ± SD; five independent experiments. Differences between WT and mutant Cav1 constructs were analyzed statistically by one-way ANOVA using SigmaPlot; $*p < 0.05$. (C, D) HEK cells expressing the YFP- and CFP-conjugated FRET pairs of either WT-Cav1 or Y14F-Cav1 were additionally transfected with unconjugated FRB and RapR-Src constructs for expression of rapamycin-activatable Src. The real-time changes in FRET/CFP intensity were recorded as described before and after treatment with 0.5 µM rapamycin. (C) Left, FRET/CFP fluorescence changes in Cav1 with respect to time, before and after addition of rapamycin to activate RapR-Src. Right, bar graph summary of FRET index values at 1, 5, and 9 min (i.e., before and after rapamycin treatment). (D) Left, trace showing the number of Cav1+ fluorescent vesicles with respect to time, before and after RapR-Src activation. Right, bar graph depicting the number of vesicles at 1, 5, and 9 min for WT-Cav1 and Y14F mutant. Representative of three separate experiments; mean ± SD.

volume of trafficking vesicles. This observation was further substantiated by data generated with the Y14D-Cav1 mutant, for which substitution of Y14 with a negatively charged aspartic acid residue (Y14D) to mimic phosphotyrosine also dissociated readily into monomers in nonboiled SDS–PAGE gels, formed larger vesicles, and exhibited lower FRET efficiency, thus implying separation between phosphorylated Cav1 molecules within the oligomeric caveolin complex. Although it is known that oligomerization of Cav1 is required for caveolae formation (Monier *et al.*, 1995; Bakhshi *et al.*, 2013; Ariotti *et al.*, 2015), we propose here that the opposite process, that is, destabilization of Cav1 oligomers after Cav1 Tyr-14 phosphorylation, is required for volume expansion to accommodate cargo and facilitate detachment of caveolae from the plasma membrane. Of interest, as shown previously (Joshi *et al.*, 2012; Orlichenko *et al.*, 2006), we too observed increased expression of endogenous Cav1 and cavin-1/PTRF in RLMVECs stably expressing Cav1-Y14D but not WT or Y14F Cav1 (Figure 2D).

Spinning-disk confocal microscopy observations were consistent with previous electron microscopy studies (Nomura and Fujimoto, 1999; Aoki *et al.*, 1999), which showed an increase in number and volume of cytoplasmic vesicles that were positive for

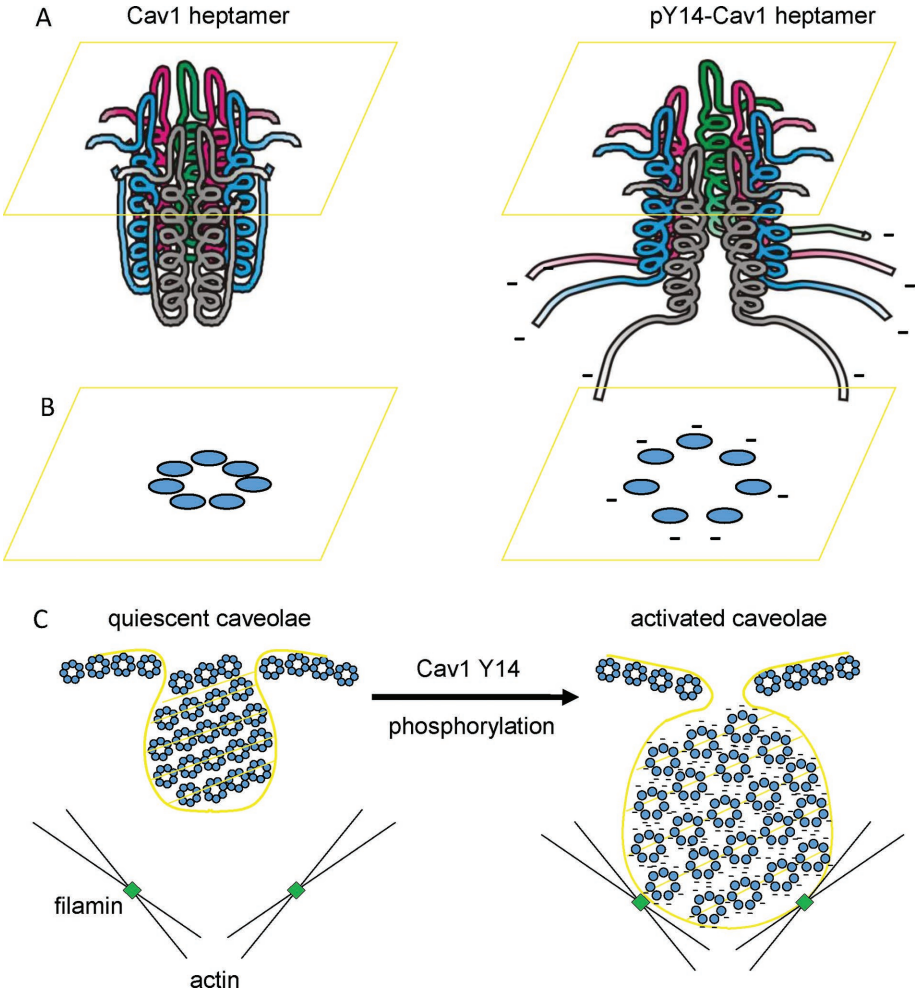

FIGURE 10: Schematic diagrams showing the effect of Cav1 phosphorylation on the activation and expansion of Cav1-positive vesicles. (A) Possible tertiary arrangement of Cav1 oligomers. Cav1 self-associates via lateral interactions between scaffolding domains (CSDs) of neighboring Cav1 molecules to form a heptameric ring imbedded in the plasma membrane via transmembrane insertion domains and palmitoylated C-terminal cysteines. Phosphorylation of Y14 leads to a conformational change and spatial separation of neighboring Cav1 molecules within the oligomer, which is presumably less stable as an oligomer in SDS–PAGE gels. (B) Top view of the heptameric ring before and after phosphorylation (indicated by negative charges). (C) Diagram depicting quiescent caveolae hanging off the plasma membrane (left). As Cav1 becomes phosphorylated on Tyr-14 (activated caveolae; right), this leads to separation of Cav1 molecules in the heptameric ring, which allows for the expansion and swelling of caveolae, most likely via binding to actin-cross-linking protein filamin A.

phospho-Cav1 by immuno-EM. Cav1 vesicle swelling can be explained by charge repulsion between the negatively charged phosphate groups on neighboring Cav1 molecules (Figure 10), which would promote separation of individual caveolin-1 molecules in the oligomer, as reported here. This observation is consistent with the observations made by Li *et al.* (2001), who demonstrated Cav1-GFP dequenching, and by our group, which demonstrated a shift from oligomer to monomer (Bakhshi *et al.*, 2013), in the presence of an NO donor.

Unlike the orchestrated membrane deformation and invagination that takes place during clathrin-dependent endocytosis, caveolae are believed to exist as preformed endocytic pits hanging from the plasma membrane and functioning to move macromolecular cargo in a "kiss-and-run" manner (Tagawa *et al.*, 2005; Pelkmans and Helenius, 2002). Cav1 oligomers, stabilized by cavin-1 (Kovtun *et al.*, 2014), may have an important function in negatively regulating caveolae internalization, thereby stabilizing caveolae at the plasma membrane. Cavin-1 dissociation from caveolae upon mechanical stress (Sinha *et al.*, 2011) and its absence from mobile cytoplasmic vesicles positive for Cav1 (Hill *et al.*, 2008) are both consistent with this hypothesis. Expansion in size via spatial separation of Cav1 molecules in the oligomeric complex would appear to be an essential component of caveolae-mediated endocytosis of albumin and insulin, which are known to act as ligands to induce their transport through the endothelium via transcytosis (Minshall *et al.*, 2000; John *et al.*, 2003; Wang *et al.*, 2015).

The idea that the caveolar scaffold acts to compartmentalize or inhibit signaling (Okamoto *et al.*, 1998) has been largely supported, and we now appreciate that modification to Cav1 can affect binding to various client proteins (Chen *et al.*, 2012). For example, we showed that pY14-Cav1 is more effective at binding and inactivating endothelial nitric oxide synthase (eNOS; Chen *et al.*, 2012), that pY14-Cav1 specifically interacts with filamin A to enhance movement of caveolae away from the plasma membrane (Sverdlov *et al.*, 2009), and that pY14-Cav1 mediates the recruitment of C-terminal Src kinase (Csk) to inactivate Src (Place *et al.*, 2011). On the basis of the distinct set of proteins that bind to either phosphorylated or nonphosphorylated Cav1, but not both, we suggested that Cav1 phosphorylation leads to a conformational change in the N-terminus that exposes an otherwise hidden or masked epitope (Chen *et al.*, 2012). Using a combination of EM, circular dichroism, and analytical ultracentrifugation, Fernandez *et al.* (2002) reported that in the WT Cav1, the first 78 amino acids wrap around an α-helix formed by the scaffolding domain. Therefore it is possible that phosphorylation of Y14 leads to separation of the N-terminus from the α-helix to expose the scaffolding domain, thereby enabling binding of proteins such as eNOS (Chen *et al.*, 2012; Trane *et al.*, 2014), whereas other proteins, such as filamin A and Csk, may bind directly to pY14-Cav1 (van Deurs *et al.*, 2003). In any case, it is interesting to speculate that Cav1 phosphorylation acts as a "switch" and becomes an important determinant of endocytic trafficking, as well as of cellular signaling. Determination of the structure of the N-terminus of Y14F and Y14D Cav1 by nuclear magnetic resonance and x-ray crystallography would likely answer this important question.

Although our studies focus on the rapid effect of Cav1 phosphorylation on the structure of the oligomeric coat, one cannot dismiss that some of our observations, especially in stably transfected RLMVECs, likely reflect increased biogenesis of caveolae mediated by phospho-Y14 Cav1. A conformational or biophysical change in Cav1 induced by phosphorylation appears to have an acute effect that leads to

internalization of caveolar vesicles and, if persistent, can promote biogenesis of caveolae. These two effects of phosphorylation are likely to be additive, as stable Y14D-Cav1 cell lines exhibit both increased trafficking dynamics and caveolae number; nonetheless, we confirmed our findings with endogenous Cav1 (Figures 1, 6, and 7).

Although the key role of Src-dependent Cav1 phosphorylation in promoting caveolae release from the plasma membrane via phosphorylation-dependent destabilization of Cav1 oligomers was demonstrated, Src may also regulate other steps involved in endocytosis. For example, Src participates in actin cytoskeletal remodeling by regulating the actin-binding protein cortactin (McNiven *et al.*, 2000; Cao *et al.*, 2003; Krueger *et al.*, 2003) and recruitment of actin the cross-linking protein filamin A to phospho-Cav1 (van Deurs *et al.*, 2003; Sverdlov *et al.*, 2009). Src thus appears to control the interaction of actin with Cav1, thereby regulating caveolae detachment from the plasma membrane and movement along actin filaments (Krueger *et al.*, 2003; Mundy *et al.*, 2002; van Deurs *et al.*, 2003; Sverdlov *et al.*, 2009). In addition, Csk, which is recruited to phosphorylated Cav1, thereby positioning it to phosphorylate Src Tyr-527 and turn it off (Cao *et al.*, 2002; Place *et al.*, 2011), and SHP-2 tyrosine phosphatase, which can dephosphorylate phospho-Cav1 (Jo *et al.*, 2014) and prolong Src signaling (Ren *et al.*, 2004), are likely to be critical regulators of caveolar internalization and transcytosis. Further study is required to fully understand the functional dynamics of Csk- and SHP-2–dependent regulation of caveolin-1 phosphorylation and of dynamic actin remodeling via association of phospho-Cav1 with filamin A in the regulation of caveolae-mediated endocytosis and transcytosis.

MATERIALS AND METHODS

Cell cultures

Early passage (4–8) HLMVECs from Lonza (Walkerville, MD) were seeded on 0.2% gelatin-coated dishes in endothelial basal medium 2 (EBM2) supplemented with EGM-2-MV BulletKit (Lonza), 10% FBS, 10 mM 4-(2-hydroxyethyl)-1-piperazineethanesulfonic acid (HEPES), and penicillin/streptomycin. RLMVECs (passages 12–20) from Vec Technologies (Rensselaer, NY) and HEK 293 cells (American Type Culture Collection, Manassas, VA) were grown in DMEM (GIBCO, Lombard, IL) supplemented with 10% FBS, 10 mM HEPES, penicillin/streptomycin, and, as required to maintain stable expression, G418 (GIBCO).

Isolation of *Cav1*$^{-/-}$ mouse lung endothelial cells

Cav1$^{-/-}$ mice obtained from Jackson Labs (Farmington, CT) were used to isolate lung endothelial cells according to an approved Institutional Animal Care and Use protocol. Neonatal mouse lungs (3 d postnatal) were used to generate highly enriched MLEC cultures by magnetic bead separation with anti-CD31 Ab as described (Tiruppathi *et al.*, 2000; Sverdlov *et al.*, 2009). The isolated endothelial cells, positive for acetylated low-density lipoprotein, platelet endothelial cell adhesion molecule 1, and angiotensin-converting enzyme, were grown on 0.1% gelatin-coated tissue culture plates or glass coverslips in EGM-2 containing 15% FBS and 20 mg/ml endothelial cell growth supplement and used at passage 2.

Reagents

All reagents were obtained from Sigma-Aldrich (Milwaukee, WI) unless stated otherwise. PP2 and *N*-nitro-L-arginine methyl ester hydrochloride were obtained from Calbiochem (San Diego, CA), and ODG was purchased from RPI (Mt. Prospect, IL). Caveolin-1 pAb and pY14-caveolin-1 mAb were from BD Biosciences (San Jose, CA), β-actin and normal mouse immunoglobulin G (IgG mouse) were obtained from Santa Cruz Biotechnology (Santa Cruz, CA), and pY118-paxillin was obtained from Thermo Scientific (Waltham, MA). 4,6-Diamidino-2-phenylindole (DAPI), Alexa 488– and Alexa568–labeled BSA, and all fluorescently labeled secondary antibodies were purchased from Invitrogen (Waltham, MA). Horseradish peroxidase–conjugated goat anti-mouse and goat anti-rabbit secondary antibodies were from Kirkegaard and Perry Laboratories (Gaithersburg, MD).

Cloning of caveolin-1 constructs

Human caveolin-1 WT cDNA in pcDNA 3.1 (Minshall *et al.*, 2000) was subcloned into pcDNA 6 containing Myc and histidine tags and used as a template to generate mutants Y14F, Y14D, and C156S using a two-step PCR protocol as described (Andersson *et al.*, 1998). Primer pairs were designed and used to introduce site-specific mutations in codons 14 and 156 (see the following list). To generate the Y14D mutation, two separate reactions with primer pairs 1/4 and 2/3 were used to introduce site-specific mutations in codon 14 while amplifying either the region 5′ or 3′ of the base pair change. The resulting PCR products were gel purified and used as overlapping templates in the second-step reaction with primer pair 1/2 to generate the full-length Y14D mutant. The Y14F and C156S constructs were generated similarly using primer pairs 1/6 and 2/5 for the Y14F mutation and 1/8 and 2/7 for the C156S mutation. All constructs were sequenced to confirm presence of mutations. We used the following primers pairs:

1. Forward WT-Cav, 5′-CTAGGTACCCAGCATGTCTGGGGGC-AAAT-3′
2. Reverse WT-Cav, 5′-CCTAGGCCTCGAGTATTTCTTTCTGCAA-GTTG-3′
3. Forward Y14D, 5′-GGACATCTCGACACCGTTCCCAT-3′
4. Reverse Y14D, 5′-ATGGGAACGGTGTCGAGATGTCC-3′
5. Forward Y14F, 5′-GGACATCTCTTTACCGTTCCCAT-3′
6. Reverse Y14F, 5′-ATGGGAACGGTAAAGAGATCTCC-3′
7. Forward C156S, 5′-CACACCGTCTCTGACCCACTC-3′
8. Reverse C156S, 5′-GAGTGGGTCAGAGACGGTGTG-3′

To generate C-terminal–tagged EGFP, EYFP, and ECFP Cav1 constructs for 4D TIRF and for FRET experiments (referred to, respectively, as Cav1-GFP, Cav1-YFP, and Cav1-CFP), we subcloned Cav1 into pEYFP-N1 or pEGFP-N1 and pAmCyan vectors (Clontech, Mountain View, CA) via restriction sites 5′-*Nhe*I and 3′-*Kpn*I and sequenced them. To obtain YPET and CyPET-tagged WT-Cav1 constructs, we amplified YPET and CyPET (AddGene, Cambridge, MA) from the original vectors by PCR with addition of *Bam*HI and *Not*I restriction sites. PCR products were then digested and subcloned into WT-Cav1 pEYFP-N1 vector previously digested with *Bam*HI and *Not*I enzymes, so that the EYFP tag was excised and substituted with either CyPET or YPET. Substitution of tags was verified by sequencing.

Cell transfections

Transfection of cDNA was performed by electroporation using an Amaxa Nucleofection kit (Amaxa, Gaithersburg, MD) or by Lipofectamine 2000 reagent (Invitrogen), according to manufacturer's instructions. Cells were used for experiments 24–48 h after transfection.

Cell treatments

Cells were washed with 37°C Dulbecco's phosphate buffered solution (DPBS) buffer supplemented with calcium and magnesium,

followed by starvation in serum-free growth medium for 3 h. As indicated, cells were pretreated with 25 μM Na_3VO_4 or 10 μM PP2 for 15 min before stimulation with BSA (3 mg/ml) for 20 min. Cells were placed on ice and washed once with ice-cold phosphate-buffered saline (PBS), three times with acid wash buffer (0.2 M acetic acid and 0.5 M NaCl, pH 2.5), and once with PBS before performing cell lysis.

Western blot analysis

For Western blotting, samples were lysed on ice in the presence of protease inhibitors (P8340; Sigma-Aldrich) and phosphatase inhibitor cocktails 2 and 3 (P5726 and P0044; Sigma-Aldrich). The less stringent sample preparation conditions included mechanical disruption of cells by passage through a 21-gauge needle in HB buffer (20 mM Tris-HCl, pH 7.4, 150 mM NaCl, 1 mM EDTA) supplemented with 2% ODG. The unbroken cells and nuclei were removed by low spin (500 × *g* for 10 min), and supernatants were taken for determination of protein concentration by the BCA Protein Assay Kit (Pierce, Rockford, IL). Samples for Western blotting were prepared in NuPage sample buffer with or without dithiothreitol (DTT; nonreducing conditions) and heated at 60°C for 10 min before loading. The more stringent ("standard") sample preparation conditions included solubilization in 1× RIPA buffer (BP-115; Boston BioProducts, Ashland, MA), followed by disruption with sonication (Sonic Dismembrator 100; Fisher Scientific, Hanover Park, IL). Under stringent conditions, samples were made in 1× Laemmli sample buffer (#161-0747; Bio-Rad, Hercules, CA) supplemented with 10 mM DTT and boiled (100°C for 5 min) before loading onto the gels. Proteins were then separated on either 12% SDS–PAGE gel or NuPage gradient gel using appropriate running and transfer buffers (Novex, Waltham, MA).

Immunoprecipitation

Cells from at least one confluent 100-mm dish were collected and solubilized in HB buffer supplemented with 2% ODG plus protease and phosphatase inhibitors as described. All insoluble materials were removed by centrifugation at 10,000 rpm (5415R; Eppendorf) for 10 min. The soluble supernatant was collected, and a 10% aliquot was saved for input analysis by Western blot. The rest of supernatant was incubated with 5 μg of primary anti-Myc antibody (ab9106; Abcam) O/N at 4°C with end-over-end rotation, followed by incubation with protein A/G agarose beads (Santa Cruz Biotechnology) for 1 h with rotation at 4°C. Beads were spun down and washed three times with ice-cold ODG lysis buffer, once with high-salt buffer (0.5 M NaCl), and once with PBS. Proteins were eluted from the beads by incubation for 20 min with 1× Laemmli sample buffer supplemented with DTT, followed by boiling at 100°C for 5 min. Samples were run on SDS–PAGE gels for Western blot analysis.

Fractionation by density gradient centrifugation

Fractionation was conducted as described previously (Macdonald and Pike, 2005) with modifications. In brief, two confluent 10-cm plates were washed with PBS and scraped into 0.6 ml of ice-cold homogenization buffer (25 mM MES [2-(*N*-morpholino)ethanesulfonic acid], pH 6.5, 150 mM NaCl, 60 mM *n*-octylglucoside with protease inhibitors). Cells were broken using a Dounce homogenizer, followed by passage through a 21-gauge needle. Homogenates were spun briefly at 500 × *g* to remove unbroken cells, and the cleared supernatant was loaded on top of 4.2 ml of a 5–30% sucrose gradient prepared in the same lysis buffer and centrifuged in SW55Ti rotor (Beckman, Indianapolis, IN) for 16 h at 50,000 rpm. Eleven equal fractions were collected from the top of the gradient, and samples were separated by SDS–PAGE gels, followed by Western blotting with anti–caveolin-1 Ab or anti–phosphoY14-caveolin-1 Ab.

Isolation of cytosolic and membrane fractions

To separate soluble and insoluble fractions, cells were grown to confluence on 10-cm plates, starved, and treated as indicated. Cells were then placed on ice, washed twice with PBS and/or acid wash buffer (if BSA treated), scraped, pelleted at 500 × *g* for 10 min, and stored at –20°C. Cell pellets were thawed and suspended in ice-cold, detergent-free buffer (10 mM Tris-HCl, pH 7.4, 2 mM EDTA, 250 mM sucrose) supplemented with protease and phosphatase inhibitor cocktails. Cells were broken by Dounce homogenizer or by passing through a 27-gauge needle. Unbroken cells and nuclei were removed by centrifugation at 500 × *g* for 10 min. The clarified supernatant was spun in a TLA-55 rotor (Beckman) for 30 min at 50,000 rpm. The pellets corresponding to the membrane fraction (insoluble proteins) and the supernatant (cytosolic proteins and microvesicles) were adjusted to the same concentration in HB buffer supplemented with 2% ODG and then analyzed by Western blotting.

Antennapedia-conjugated CSD peptide

A peptide corresponding to the CSD (amino acids 82–101) was synthesized (bioWORLD, Dublin, OH) as a biotin-labeled conjugate together with the Antp internalization sequence as described (Bucci *et al.*, 2000). Characterization of the dose and time dependence of peptide internalization in cultured RLMVEC indicated that maximal uptake was achieved by 1 h of incubation at 37°C with 5 μM peptide. Control experiments used the biotin-labeled Antp peptide without the CSD.

RapR-Src activation

RapR-Src and mCherry FRB retroviral constructs were generated as described (Chu *et al.*, 2014). HLMVEC cells (Lonza) were infected with RapR-Src and FRB viral supernatants for 24 h, after which the cells were starved and stimulated with 0.5 μM rapamycin to activate Src for 0–60 min.

^{125}I-albumin uptake and transendothelial transport

Confluent cells were serum starved for 3 h and then incubated at 37°C with 0.1 mg/ml of tracer-labeled ^{125}I-albumin (PerkinElmer-Cetus, Waltham, MA) in the presence or absence of 100 mg/ml of unlabeled albumin to measure total versus nonspecific uptake as previously described (John *et al.*, 2003). Uptake assays were stopped by placing cells on ice and adding ice-cold Hanks balanced salt solution (HBSS) followed by two additional washes with ice-cold HBSS and two washes with acid wash buffer (0.2 M acetic acid and 0.5 M NaCl, pH 2.5) to remove cell surface–bound ^{125}I-albumin. Cells were then lysed, resuspended, and transferred to vials for γ counting to determine the amount of radioactivity (counts per minute [cpm]) inside the cells. For measurement of transendothelial (vesicle-mediated) permeability of ^{125}I-albumin across RLMVEC monolayers, cells were grown on porous Transwell filter inserts (12-mm diameter, 1-cm^2 growth area, 0.4-μm pore size; Corning Costar, Cambridge, MA) until fully confluent. Where indicated, cells were washed with PBS and loaded for 1 h at 37°C with 5 μM Antp-CSD peptide or Antp alone, followed by extensive washes with PBS. Cells were then starved for 3 h in serum-free growth medium. The transcytosis assay was performed by adding 0.1 mg/ml albumin labeled with 1 × 10^5 cpm ^{125}I-albumin in the presence or absence of unlabeled 100 mg/ml albumin

added to the upper chamber of Transwells. The amount of ^{125}I-albumin transported from the top to the bottom chamber across the RLMVEC monolayer was then measured as described previously (John *et al.*, 2003).

Alexa 488–BSA uptake

Confluent *Cav1*$^{-/-}$ MLECs were washed with PBS, incubated for 3 h in serum-free medium, and incubated with Alexa 488–conjugated albumin (0.1 mg/ml Alexa 488–BSA [Invitrogen] mixed into 1 mg/ml of nonfluorescent BSA in HEPES-buffered HBSS solution for 30 min at 37°C. Subsequently the cells were washed extensively with ice-cold PBS, followed by acid wash buffer (0.2 M acetic acid and 0.5 M NaCl, pH 2.5) to remove noninternalized/membrane-associated albumin. The cells were then fixed, permeabilized, and stained with anti-Myc or anti-caveolin pAb and the nuclear marker DAPI (Shajahan *et al.*, 2004a). Nonconfocal DAPI images were acquired using Hg-lamp excitation and an ultraviolet filter set; confocal microscopy was performed using a Zeiss LSM 510 META system with a 100×/1.45 numerical aperture (NA) AlphaFluor objective and 488/543-nm excitation laser lines. Fluorescence emission was detected in optical sections of <1-μm thickness (pinhole set to achieve 1 Airy unit) separately for each fluorophore using a multitrack configuration.

Spinning-disk confocal microscopy

Cav1$^{-/-}$ mouse and normal RLMVECs were grown in collagen-coated, 25-mm MatTek (Ashland, MA) dishes and transfected with Cav1-GFP constructs in pcDNA6.1 by Amaxa Nucleofector for 24 h and then starved for 3 h in serum-free growth medium. A dual spinning-disk confocal (Yokogawa CSU10) scanning head (Ultraview; PerkinElmer-Cetus) mounted on a Nikon TE 2000 inverted microscope with 100×/1.4 NA objective and Orca-ER charge-coupled device camera (Hamamatsu, Bridgewater, NJ) was used. The 4D dynamics (*x*, *y*, *z*, time) of Cav1+ vesicle trafficking (50- to 100-ms exposure time, *z*-step increment of 0.2 μm, pixel size of 0.067 μm) was assessed at a frame rate for the acquisition of 200 ms/slice and analyzed by Volocity particle-tracking software (ImproVision, Boston, MA). We used 3D deconvolution (with no filter) to reduce noise, resulting in better classification and higher resolution.

Live-cell FRET

HEK cells cultured on poly-D-lysine–treated, glass-bottom dishes (MatTek) were cotransfected with Cav1 cDNAs used as the donor (Cav1-CFP) and acceptor (Cav1-YFP) to create FRET pairs, using Lipofectamine2000 (Life Technologies, Carlsbad, CA). At 24 h posttransfection, cells were starved for 3 h in serum-free, phenol red-free DMEM and then transferred to a Zeiss LSM-710 confocal microscope (binary GaAsP [BIG]) system equipped with PeCon heated stage and CO_2 controller and GaAsP detector (Zeiss). Before the FRET measurements, cells were scanned with 458- and 514-nm lasers to determine cellular localization and equivalent expression of ECFP-tagged and EYFP-tagged constructs, respectively. FRET images from ROIs situated in peripheral regions of the cell were generated with the 458-nm laser line and emission detection spanning 463–516 nm for CFP and 526–608 nm for YFP (FRET) in optical sections of <3.3 μm. Experiments began after thermal equilibration in the environmental PeCon chamber and stabilization of the basal fluorescence signal (~20 min). Basal FRET and CFP emission spectra were collected for at least 5 min before addition of BSA (3 mg/ml) and continued for an additional 20–30 min after the stimulus. ImageJ (Fiji) was used to quantify fluorescence intensities (YFP and CFP) at each time point, with threshold operation to exclude background and overexposed areas. Changes in FRET were monitored by calculating the FRET index (Shrestha *et al.*, 2015), determined by dividing by FRET (YFP) intensity by CFP emission at each time point to account for temporal fluctuations. FRET index before stimulation was subsequently normalized to 1, and changes after BSA stimulation are represented as its fraction. The number of fluorescent vesicles at each time point was quantified by Imaris 7.1 software. Cells cotransfected with pEYFP-N1/pAmCyan empty vectors were used as negative experimental controls and for determination of optimal conditions for minimizing photobleaching of fluorophores with time.

FRET efficiency

CFP- and YFP-tagged constructs of Cav1 were cotransfected into HEK cells grown in MatTek glass-bottom dishes. At 24 h posttransfection, cells were serum starved for 3 h in phenol red–free DMEM, fixed for 20 min in 4% paraformaldehyde in HBSS buffer, and mounted in ProLong Antifade Mounting Medium (Molecular Probes). All images were collected with a Zeiss LSM-710 confocal microscope (BIG) system and analyzed using Zeiss Zen Blue edition software. Prebleach and postbleach donor fluorescence (CFP) were measured using 458-nm excitation (458/514 nm dual dichroic) and emission at 463–516 nm (CFP emission range). Photobleaching of the acceptor (YFP) in selected regions ROIs was performed by excitation at 514 nm at 100% laser intensity for 30 iterations, and then postbleach CFP images were captured immediately. FRET efficiency was calculated according to the formula $E_{FRET} = (I_D - I_{AD})/I_D$, where I indicates fluorescence intensity of the donor (D) in the presence (I_{AD}) or absence (I_D) of the acceptor (A), that is, CFP intensity before and after photobleaching YFP.

TIRF microscopy and quantification

Cells were transfected with Cav-1–GFP constructs or GFP alone (negative control) and plated onto gelatin-coated, glass-bottomed dishes (MatTek). At 48 h after transfection, cells were subjected to TIRF analysis using an Axio Observer Z1 inverted microscope equipped with Dynamic Laser TIRF module (Carl Zeiss MicroImaging) and ORCA-II ERG charge-coupled device camera (Hamamatsu). Dynamics of Cav-1–GFP was acquired with a 100×/1.45 NA alpha Plan Fluar oil immersion objective at 37°C. Images (200-ms exposure and 1-s frame rate) were collected, and dynamic events in TIRF plane were quantified from thresholded *z*-projections (16 cells/group, three or four areas/cell) using the ImageJ Particle Analysis plug-in. For quantification, areas free of large fluorescent aggregates of Cav-1–GFP were selected. Results are presented as the percentage of the number of events detected in the TIRF plane over 30 frames (i.e., 30 s) per unit area.

Transmission electron microscopy

For ultrastructural analysis, cells grown on Matrigel-coated plastic dishes were fixed with Karnovsky fixative, stained with OsO_4, dehydrated, and embedded in Epon. Ultrathin sections (40 μm) were stained with uranyl acetate and lead citrate and examined under a transmission electron microscope (Jeol 1220), as described previously (Bakhshi *et al.*, 2013).

Statistical analysis

Statistical comparisons for nonparametric distribution of Cav1 vesicles were done by Kolmogorov–Smirnov test, and all other analyses were made with GraphPad Prism (La Jolla, CA) or Sigma Plot (San Jose, CA) software using two-tailed analysis of variance (ANOVA); the significance level was set at $p < 0.05$; all experiments were performed at least in triplicate.

ACKNOWLEDGMENTS

We acknowledge Maricela Castellon (Minshall lab), Linda Juarez (Research Resources Center Electron Microscopy Core), and Ke Ma (Research Resources Center Confocal Microscopy Core) for excellent technical support. This research was supported in part by the Francis Families Foundation (R.D.M.), Illinois Research Initiative in Biotechnology (R.D.M., A.B.M.), and National Institutes of Health Grants R01 HL71626 (R.D.M.), T32 HL07239 (A.B.M.), R21 CA159179 (A.K.V.), and P01 HL60678 (R.D.M., C.T., A.B.M.).

REFERENCES

Ahn S, Maudsley S, Luttrell LM, Lefkowitz RJ, Daaka Y (1999). Src-mediated tyrosine phosphorylation of dynamin is required for beta2-adrenergic receptor internalization and mitogen-activated protein kinase signaling. J Biol Chem 274, 1185–1188.

Anderson RG (1998). The caveolae membrane system. Annu Rev Biochem 67, 199–225.

Andersson E, Hellman L, Gullberg U, Olsson I (1998). The role of the propeptide for processing and sorting of human myeloperoxidase. J Biol Chem 273, 4747–4753.

Aoki T, Nomura R, Fujimoto T (1999). Tyrosine phosphorylation of caveolin-1 in the endothelium. Exp Cell Res 253, 629–636.

Ariotti N, Rae J, Leneva N, Ferguson C, Loo D, Okano S, Hill MM, Walser P, Collins BM, Parton RG (2015). Molecular characterization of caveolin-induced membrane curvature. J Biol Chem 290, 24875–24890.

Bakhshi FR, Mao M, Shajahan AN, Piegeler T, Chen Z, Chernaya O, Sharma T, Elliott WM, Szulcek R, Bogaard HJ, *et al.* (2013). Nitrosation-dependent caveolin 1 phosphorylation, ubiquitination, and degradation and its association with idiopathic pulmonary arterial hypertension. Pulm Circ 3, 816–830.

Bucci M, Gratton JP, Rudic RD, Acevedo L, Roviezzo F, Cirino G, Sessa WC (2000). In vivo delivery of the caveolin-1 scaffolding domain inhibits nitric oxide synthesis and reduces inflammation. Nat Med 6, 1362–1367.

Cao H, Courchesne WE, Mastick CC (2002). A phosphotyrosine-dependent protein interaction screen reveals a role for phosphorylation of caveolin-1 on tyrosine 14: recruitment of C-terminal Src kinase. J Biol Chem 277, 8771–8774.

Cao H, Orth JD, Chen J, Weller SG, Heuser JE, McNiven MA (2003). Cortactin is a component of clathrin-coated pits and participates in receptor-mediated endocytosis. Mol Cell Biol 23, 2162–2170.

Chen Z, Bakhshi FR, Shajahan AN, Sharma T, Mao M, Trane A, Bernatchez P, van Nieuw Amerongen GP, Bonini MG, Skidgel RA, *et al.* (2012). Nitric oxide-dependent Src activation and resultant caveolin-1 phosphorylation promote eNOS/caveolin-1 binding and eNOS inhibition. Mol Biol Cell 23, 1388–1398.

Chu PH, Tsygankov D, Berginski ME, Dagliyan O, Gomez SM, Elston TC, Karginov AV, Hahn KM (2014). Engineered kinase activation reveals unique morphodynamic phenotypes and associated trafficking for Src family isoforms. Proc Natl Acad Sci USA 111, 12420–12425.

Fernandez I, Ying Y, Albanesi J, Anderson RG (2002). Mechanism of caveolin filament assembly. Proc Natl Acad Sci USA 99, 11193–11198.

Glenney JR Jr, Zokas L (1989). Novel tyrosine kinase substrates from Rous sarcoma virus-transformed cells are present in the membrane skeleton. J Cell Biol 108, 2401–2408.

Gottlieb-Abraham E, Shvartsman DE, Donaldson JC, Ehrlich M, Gutman O, Martin GS, Henis YI (2013). Src-mediated caveolin-1 phosphorylation affects the targeting of active Src to specific membrane sites. Mol Biol Cell 24, 3881–3895.

Hill MM, Bastiani M, Luetterforst R, Kirkham M, Kirkham A, Nixon SJ, Walser P, Abankwa D, Oorschot VM, Martin S, *et al.* (2008). PTRF-cavin, a conserved cytoplasmic protein required for caveola formation and function. Cell 132, 113–124.

Hill MM, Scherbakov N, Schiefermeier N, Baran J, Hancock JF, Huber LA, Parton RG, Parat MO (2007). Reassessing the role of phosphocaveolin-1 in cell adhesion and migration. Traffic 8, 1695–1705.

Hu G, Place AT, Minshall RD (2008a). Regulation of endothelial permeability by Src kinase signaling: vascular leakage versus transcellular transport of drugs and macromolecules. Chem Biol Interact 171, 177–189.

Hu G, Ye RD, Dinauer MC, Malik AB, Minshall RD (2008b). Neutrophil caveolin-1 expression contributes to mechanism of lung inflammation and injury. Am J Physiol Lung Cell Mol Physiol 294, L178–L186.

Jo A, Park H, Lee SH, Ahn SH, Kim HJ, Park EM, Choi YH (2014). SHP-2 binds to caveolin-1 and regulates Src activity via competitive inhibition of CSK in response to H2O2 in astrocytes. PLoS One 9, e91582.

John TA, Vogel SM, Minshall RD, Ridge K, Tiruppathi C, Malik AB (2001). Evidence for the role of alveolar epithelial gp60 in active transalveolar albumin transport in the rat lung. J Physiol 533, 547–559.

John TA, Vogel SM, Tiruppathi C, Malik AB, Minshall RD (2003). Quantitative analysis of albumin uptake and transport in the rat microvessel endothelial monolayer. Am J Physiol Lung Cell Mol Physiol 284, L187–L196.

Joshi B, Bastiani M, Strugnell SS, Boscher C, Parton RG, Nabi IR (2012). Phosphocaveolin-1 is a mechanotransducer that induces caveola biogenesis via Egr1 transcriptional regulation. J Cell Biol 199, 425–435.

Kovtun O, Tillu VA, Jung W, Leneva N, Ariotti N, Chaudhary N, Mandyam RA, Ferguson C, Morgan GP, Johnston WA, *et al.* (2014). Structural insights into the organization of the cavin membrane coat complex. Dev Cell 31, 405–419.

Krueger EW, Orth JD, Cao H, McNiven MA (2003). A dynamin-cortactin-Arp2/3 complex mediates actin reorganization in growth factor-stimulated cells. Mol Biol Cell 14, 1085–1096.

Kurzchalia TV, Dupree P, Parton RG, Kellner R, Virta H, Lehnert M, Simons K (1992). VIP21, a 21-kD membrane protein is an integral component of trans-Golgi-network-derived transport vesicles. J Cell Biol 118, 1003–1014.

Lee H, Woodman SE, Engelman JA, Volonte D, Galbiati F, Kaufman HL, Lublin DM, Lisanti MP (2001). Palmitoylation of caveolin-1 at a single site (Cys-156) controls its coupling to the c-Src tyrosine kinase: targeting of dually acylated molecules (GPI-linked, transmembrane, or cytoplasmic) to caveolae effectively uncouples c-Src and caveolin-1 (TYR-14). J Biol Chem 276, 35150–35158.

Li H, Brodsky S, Basco M, Romanov V, De Angelis DA, Goligorsky MS (2001). Nitric oxide attenuates signal transduction: possible role in dissociating caveolin-1 scaffold. Circ Res 88, 229–236.

Li S, Couet J, Lisanti MP (1996a). Src tyrosine kinases, Galpha subunits, and H-Ras share a common membrane-anchored scaffolding protein, caveolin. Caveolin binding negatively regulates the auto-activation of Src tyrosine kinases. J Biol Chem 271, 29182–29190.

Li S, Seitz R, Lisanti MP (1996b). Phosphorylation of caveolin by src tyrosine kinases. The alpha-isoform of caveolin is selectively phosphorylated by v-Src in vivo. J Biol Chem 271, 3863–3868.

Macdonald JL, Pike LJ (2005). A simplified method for the preparation of detergent-free lipid rafts. J Lipid Res 46, 1061–1067.

Mao M, Varadarajan S, Fukai T, Bakhshi FR, Chernaya O, Dudley SC Jr, Minshall RD, Bonini MG (2014). Nitroglycerin tolerance in caveolin-1 deficient mice. PLoS One 9, e104101.

McNiven MA, Kim L, Krueger EW, Orth JD, Cao H, Wong TW (2000). Regulated interactions between dynamin and the actin-binding protein cortactin modulate cell shape. J Cell Biol 151, 187–198.

Minshall RD, Tiruppathi C, Vogel SM, Niles WD, Gilchrist A, Hamm HE, Malik AB (2000). Endothelial cell-surface gp60 activates vesicle formation and trafficking via G(i)-coupled Src kinase signaling pathway. J Cell Biol 150, 1057–1070.

Monier S, Parton RG, Vogel F, Behlke J, Henske A, Kurzchalia TV (1995). VIP21-caveolin, a membrane protein constituent of the caveolar coat, oligomerizes in vivo and in vitro. Mol Biol Cell 6, 911–927.

Mundy DI, Machleidt T, Ying YS, Anderson RG, Bloom GS (2002). Dual control of caveolar membrane traffic by microtubules and the actin cytoskeleton. J Cell Sci 115, 4327–4339.

Nomura R, Fujimoto T (1999). Tyrosine-phosphorylated caveolin-1: immunolocalization and molecular characterization. Mol Biol Cell 10, 975–986.

Okamoto T, Schlegel A, Scherer PE, Lisanti MP (1998). Caveolins, a family of scaffolding proteins for organizing "preassembled signaling complexes" at the plasma membrane. J Biol Chem 273, 5419–5422.

Orlichenko L, Huang B, Krueger E, McNiven MA (2006). Epithelial growth factor-induced phosphorylation of caveolin 1 at tyrosine 14 stimulates caveolae formation in epithelial cells. J Biol Chem 281, 4570–4579.

Parton RG, del Pozo MA (2013). Caveolae as plasma membrane sensors, protectors and organizers. Nat Rev Mol Cell Biol 14, 98–112.

Parton RG, Joggerst B, Simons K (1994). Regulated internalization of caveolae. J Cell Biol 127, 1199–1215.

Pelkmans L, Helenius A (2002). Endocytosis via caveolae. Traffic 3, 311–320.

Pelkmans L, Puntener D, Helenius A (2002). Local actin polymerization and dynamin recruitment in SV40-induced internalization of caveolae. Science 296, 535–539.

Pelkmans L, Zerial M (2005). Kinase-regulated quantal assemblies and kiss-and-run recycling of caveolae. Nature 436, 128–133.

Place AT, Chen Z, Bakhshi FR, Liu G, O'Bryan JP, Minshall RD (2011). Cooperative role of caveolin-1 and C-terminal Src kinase binding protein in C-terminal Src kinase-mediated negative regulation of c-Src. Mol Pharmacol 80, 665–672.

Predescu D, Palade GE (1993). Plasmalemmal vesicles represent the large pore system of continuous microvascular endothelium. Am J Physiol 265, H725–H733.

Predescu SA, Predescu DN, Timblin BK, Stan RV, Malik AB (2003). Intersectin regulates fission and internalization of caveolae in endothelial cells. Mol Biol Cell 14, 4997–5010.

Ren Y, Meng S, Mei L, Zhao ZJ, Jove R, Wu J (2004). Roles of Gab1 and SHP2 in paxillin tyrosine dephosphorylation and Src activation in response to epidermal growth factor. J Biol Chem 279, 8497–8505.

Rothberg KG, Heuser JE, Donzell WC, Ying YS, Glenney JR, Anderson RG (1992). Caveolin, a protein component of caveolae membrane coats. Cell 68, 673–682.

Rozelle AL, Machesky LM, Yamamoto M, Driessens MH, Insall RH, Roth MG, Luby-Phelps K, Marriott G, Hall A, Yin HL (2000). Phosphatidylinositol 4,5-bisphosphate induces actin-based movement of raft-enriched vesicles through WASP-Arp2/3. Curr Biol 10, 311–320.

Schmid SL (1997). Clathrin-coated vesicle formation and protein sorting: an integrated process. Annu Rev Biochem 66, 511–548.

Schubert W, Frank PG, Razani B, Park DS, Chow CW, Lisanti MP (2001). Caveolae-deficient endothelial cells show defects in the uptake and transport of albumin in vivo. J Biol Chem 276, 48619–48622.

Shajahan AN, Timblin BK, Sandoval R, Tiruppathi C, Malik AB, Minshall RD (2004a). Role of Src-induced dynamin-2 phosphorylation in caveolae-mediated endocytosis in endothelial cells. J Biol Chem 279, 20392–20400.

Shajahan AN, Tiruppathi C, Smrcka AV, Malik AB, Minshall RD (2004b). Gbetagamma activation of Src induces caveolae-mediated endocytosis in endothelial cells. J Biol Chem 279, 48055–48062.

Shrestha D, Jenei A, Nagy P, Vereb G, Szollosi J (2015). Understanding FRET as a research tool for cellular studies. Int J Mol Sci 16, 6718–6756.

Singh RD, Puri V, Valiyaveettil JT, Marks DL, Bittman R, Pagano RE (2003). Selective caveolin-1-dependent endocytosis of glycosphingolipids. Mol Biol Cell 14, 3254–3265.

Sinha B, Koster D, Ruez R, Gonnord P, Bastiani M, Abankwa D, Stan RV, Butler-Browne G, Vedie B, Johannes L, *et al*. (2011). Cells respond to mechanical stress by rapid disassembly of caveolae. Cell 144, 402–413.

Sun Y, Hu G, Zhang X, Minshall RD (2009). Phosphorylation of caveolin-1 regulates oxidant-induced pulmonary vascular permeability via paracellular and transcellular pathways. Circ Res 105, 676–685.

Sverdlov M, Shajahan AN, Minshall RD (2007). Tyrosine phosphorylation-dependence of caveolae-mediated endocytosis. J Cell Mol Med 11, 1239–1250.

Sverdlov M, Shinin V, Place AT, Castellon M, Minshall RD (2009). Filamin A regulates caveolae internalization and trafficking in endothelial cells. Mol Biol Cell 20, 4531–4540.

Tagawa A, Mezzacasa A, Hayer A, Longatti A, Pelkmans L, Helenius A (2005). Assembly and trafficking of caveolar domains in the cell: caveolae as stable, cargo-triggered, vesicular transporters. J Cell Biol 170, 769–779.

Tiruppathi C, Song W, Bergenfeldt M, Sass P, Malik AB (1997). Gp60 activation mediates albumin transcytosis in endothelial cells by tyrosine kinase-dependent pathway. J Biol Chem 272, 25968–25975.

Tiruppathi C, Yan W, Sandoval R, Naqvi T, Pronin AN, Benovic JL, Malik AB (2000). G protein-coupled receptor kinase-5 regulates thrombin-activated signaling in endothelial cells. Proc Natl Acad Sci USA 97, 7440–7445.

Trane AE, Pavlov D, Sharma A, Saqib U, Lau K, van Petegem F, Minshall RD, Roman LJ, Bernatchez PN (2014). Deciphering the binding of caveolin-1 to client protein endothelial nitric-oxide synthase (eNOS): scaffolding subdomain identification, interaction modeling, and biological significance. J Biol Chem 289, 13273–13283.

van Deurs B, Roepstorff K, Hommelgaard AM, Sandvig K (2003). Caveolae: anchored, multifunctional platforms in the lipid ocean. Trends Cell Biol 13, 92–100.

Vogel SM, Minshall RD, Pilipovic M, Tiruppathi C, Malik AB (2001). Albumin uptake and transcytosis in endothelial cells in vivo induced by albumin-binding protein. Am J Physiol Lung Cell Mol Physiol 281, L1512–1522.

Wang H, Wang AX, Aylor K, Barrett EJ (2015). Caveolin-1 phosphorylation regulates vascular endothelial insulin uptake and is impaired by insulin resistance in rats. Diabetologia 58, 1344–1353.

Yang KC, Rutledge CA, Mao M, Bakhshi FR, Xie A, Liu H, Bonini MG, Patel HH, Minshall RD, Dudley SC Jr (2014). Caveolin-1 modulates cardiac gap junction homeostasis and arrhythmogenecity by regulating cSrc tyrosine kinase. Circ Arrhythm Electrophysiol 7, 701–710.